JGR Space Physics

RESEARCH ARTICLE
10.1029/2020JA028605

Saturn's Nightside Ring Current During Cassini's Grand Finale

G. Provan[1], T. J. Bradley[1], E. J. Bunce[1], S. W. H. Cowley[1], H. Cao[3,4], M. Dougherty[2], G. J. Hunt[2], E. Roussos[5], N. R. Staniland[2], and C. Tao[6]

[1]School of Physics and Astronomy, University of Leicester, Leicester, UK, [2]Blackett Laboratory, Imperial College London, London, UK, [3]Department of Earth and Planetary Sciences, Harvard University, Cambridge, MA, USA, [4]Division of Geological and Planetary Sciences, California Institute of Technology, CA, USA, [5]Max Planck Institute for Solar System Research, Justus-von-Liebig-Weg 3, Göttingen, Germany, [6]National Institute of Information and Communications Technology, Koganei, Japan

Key Points:

- We study Saturn's nightside ring current during Cassini's Grand Finale
- Saturn's nightside ring current is driven jointly by the external solar wind and by the internal planetary period oscillations
- Magnetospheric storms, triggered by both the internal and external drivers, result in a partial ring current of hot plasma on the nightside

Correspondence to:
G. Provan,
gp31@le.ac.uk

Citation:
Provan, G., Bradley, T. J., Bunce, E. J., Cowley, S. W. H., Cao, H., Dougherty, M., et al. (2021). Saturn's nightside ring current during Cassini's Grand Finale. *Journal of Geophysical Research: Space Physics*, *126*, e2020JA028605. https://doi.org/10.1029/2020JA028605

Received 19 AUG 2020
Accepted 5 JAN 2021

Abstract During Cassini's Grand Finale proximal orbits, the spacecraft traversed the nightside magnetotail to ~21 Saturn radii. Clear signatures of Saturn's equatorial current sheet are observed in the magnetic field data. An axisymmetric model of the ring current is fitted to these data, amended to take into account the tilt of the current layer by solar wind forcing, its teardrop-shaped nature and the magnetotail and magnetopause fringing fields. Variations in ring current parameters are examined in relation to external driving of the magnetosphere by the solar wind and internal driving by the two planetary period oscillations (PPOs), and compared with previous dawn and dayside observations. We find that the relative phasing of the PPOs determines the ring current's response to solar wind conditions. During solar wind compressions when the PPOs are in antiphase, a thick partial ring current is formed on the nightside, dominated by hot plasma injected by tail reconnection. This partial ring current should close partly via magnetopause currents and possibly via field-aligned currents into the ionosphere. However, during solar wind compressions when the PPOs are in phase, this partial ring current is not detected. During solar wind rarefactions an equatorial "magnetodisc" configuration is observed in the dayside/dawn/nightside regions, with similar total currents flowing at these local times. During very quiet intervals of prolonged solar wind rarefaction, a thin current sheet with an enhanced current density is formed, indicative of a ring current dominated by cool, dense, Enceladus water group ions.

Plain Language Summary We have studied Saturn's nightside ring current during Cassini's Grand Finale. We find that Saturn's ring current, like Saturn's magnetosphere as a whole, is driven by factors both internal and external to the magnetosphere. The external driver is the solar wind and the internal drivers are the planetary period oscillations. Magnetospheric storms, triggered by both drivers, result in a partial ring current of hot plasma on Saturn's nightside.

1. Introduction

1.1. Saturn's Ring Current

Saturn's magnetosphere is a dynamical environment, shaped by the solar wind, the planet's fast rotation, a strong planetary magnetic field, and significant mass-loading from the moon Enceladus (Gombosi et al., 2009; Thomsen et al., 2013, and references therein). The form of Saturn's magnetosphere is determined by pressure balance at the magnetopause boundary between the internal stresses and the solar wind dynamic pressure (e.g. Russell et al., 2003). The action of centrifugal forces confines magnetospheric plasma towards the equatorial plane, resulting in the formation of a disc-like distribution of plasma through which a ring current flows in an azimuthal eastward direction. Magnetic field lines are distorted in a radial direction, and a magnetodisc structure is formed which is asymmetric in local time (Arridge et al., 2007, 2008a, 2008b; Carbary, 2019; Carbary et al., 2012; Ness et al., 1981, 1982; Sittler et al., 1983; Smith et al., 1980). The solar wind also bends Saturn's dayside and nightside ring current into a bowl shape, which was tilted south of the equatorial plane during the northern hemisphere summer conditions studied in this paper (Arridge et al., 2008b; Bunce et al., 2008; Cowley et al., 2006—see Equation 6 below).

The nature of Saturn's ring current and its modulation by the solar wind have been studied over the past 40 years using magnetic field observations (see, e.g. papers by Arridge et al., 2006, 2007, 2008a, 2008b; Alexeev et al., 2006; Bunce & Cowley, 2003; Bunce et al., 2007, 2008; Dougherty et al., 2005; Giampieri & Dougherty, 2004; Kellett et al., 2009) and the model presented by Connerney et al. (1981b, 1983) (see Section 3.1.1). This model has been fitted to magnetic field observations from Pioneer-11, the Voyagers, and Cassini spacecraft, to determine the size and strength of Saturn's ring current (Bunce & Cowley, 2003; Bunce et al., 2007; Connerney et al., 1981b, 1983; Giampieri & Dougherty, 2004). Saturn's ring current, as inferred from Voyager data, is located between 8 and 16 R_s (Saturn's 1 bar equatorial radius, R_s, is 60,268 km) in a region a few R_s wide on either side of the equatorial plane. It carries a total azimuthal current of ~10 MA (Connerney et al., 1983). Bunce et al. (2007) examined the ring current in the dayside/dawn sector using magnetic field data (B_z component only) observed on near-equatorial orbits from the first two years of the Cassini mission, combined with data from Pioneer-11 and the two Voyager spacecraft. They showed that the strength and size of the dayside/dawn ring current is strongly modulated by the solar wind dynamic pressure and the corresponding position of the magnetopause. During intervals of higher solar wind dynamic pressure, when the magnetopause is compressed inwards, the dayside/dawn ring current is smaller and less intense. For the minimum observed subsolar magnetopause distance of ~16.5 R_s , the outer radius of the ring current decreased to ~15 R_s, and the ring current's magnetic moment was ~20% of the planetary dipole moment. During solar wind rarefactions, Saturn's magnetosphere expands and a magnetodisc forms in the equatorial region at all local times with Saturn's ring current strengthening and expanding. For the maximum observed subsolar magnetopause distance of ~26 R_s, Bunce et al. (2007) found that the outer edge of the ring current expanded to ~21 R_s, and the ring current's magnetic moment to ~60% of the planetary dipole moment. The inner edge of the ring current was located at ~6.5 R_s, almost independent of solar wind dynamic pressure. These results will be compared in detail with those derived here in Section 6.2. Sorba et al. (2017) used a two-dimensional axisymmetric model of Saturn's dayside magnetosphere (Achilleos et al., 2010) to investigate the compressibility of Saturn's magnetosphere. They found that the when the solar wind dynamic pressure was low, the formation of a disc-like magnetic field structure resulted in a more compressible magnetosphere. Recent work by, for example, Sergis et al. (2017) showed that Saturn's ring current is strongly asymmetric in local time. Sorba et al. (2019) modeled the local-time variation of Saturn's magnetosphere, reporting on the variability of current sheet thickness and density with local time.

Complex plasma density models of Saturn's magnetosphere have been developed (e.g. Persoon et al., 2009, 2020; Richardson & Sittler, 1990; Sittler et al., 2008; Sergis et al., 2011). Persoon et al. (2009, 2020) provide global maps of two-species plasma distributions in Saturn's inner magnetosphere consisting of water group and hydrogen ions. The cool Enceladus water group ions, which evolve from within the inner magnetosphere and are transported radially outward, are centrifugally confined to within a few Saturn radii of the equatorial plane. The lighter hydrogen ions expand along the field lines away from the equatorial plane. The width of the plasma sheet is essentially given by the scale heights of these two species, which for a rotating plasma in a dipole field, are proportional to the square root of the ion parallel temperature and inversely proportional to the square root of the ion mass, as given by Equation 3 of Persoon et al. (2009)

$$H_i = \sqrt{\frac{2kT_{||}}{3m_i\Omega^2 R_S^2}} \tag{1}$$

where H_i is the dimensionless scale height for the ith species, m_i is the mass of the ith species, Ω is the rotation rate of the plasma and $T_{||}$ is the parallel temperature. The heavier water ions have a scale height that is half an order of magnitude lower than the hydrogen ion scale height at $L = 10$, increasing to an order of magnitude lower than the hydrogen ion scale height at $L = 2.4$ (where L is the McIlwain L-shell parameter, McIlwain, 1961). The best fit for the water group ion temperature ranges from 0.4 to 80 eV between the L-shell ranges of 2.4–10 R_s. The hydrogen ion temperature ranges from 5 to 45 eV over the same L-shell range.

Cowley et al. (2004) proposed an in-principle steady-state picture of equatorial plasma flow, described as part of a global circulation pattern that combined the Dungey and Vasyliūnas convection patterns (Dungey, 1961; Vasyliūnas, 1983). This plasma circulation is discussed here in the context of Figure 1, a schemat-

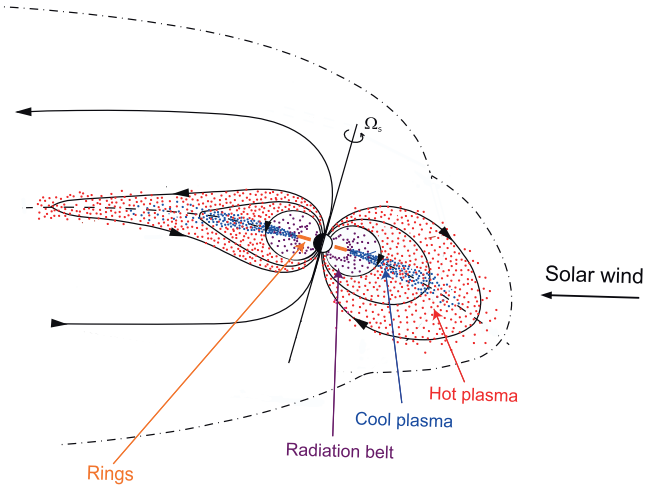

Figure 1. Schematic showing a noon-midnight cut through Saturn's magnetosphere for northern summer conditions. The solar wind is flowing from right to left and the outer dashed line represents the magnetopause boundary. The orange lines represents Saturn's ring systems. The blue dots near the equatorial plane represent the cool Enceladus water group plasma. Close to the planet, the purple dotted region represents the inner radiation belt of high-energy particles. The surrounding red dots represent a layer of hot and tenuous plasma (adapted from Kellett et al., 2009).

ic showing a noon-midnight cut through Saturn's magnetosphere. This figure was originally presented by Kellett et al. (2009), updated here for the northern summer conditions relevant for this paper. The solar wind is flowing from right to left and the outer dot-dashed line represents the magnetopause boundary. The orange lines represent Saturn's ring systems, extending to about ∼2 R_s in the equatorial plane. The blue dots represent the cool Enceladus water group plasma, centrifugally confined near the equatorial plane, which dominates a central region of circulating flow. Close to the planet, the purple dotted region represents the inner radiation belt of high-energy particles that extends from the outer edge of Saturn's main ring system. The surrounding red dots represent a layer of hot and tenuous (∼keV to several tens of keV) plasma. The boundary between the high-energy and the hot and tenuous plasma regimes occurs at ∼10 R_s, and has been described as Saturn's plasmapause (Young et al., 2005). At this boundary centrifugally-driven interchange events occur, characterized by alternating fingers of hot (<∼50 keV), tenuous inward-moving plasma and cold, dense outward-moving plasma (Southwood & Kivelson, 1987; Mauk et al., 2009; Thomsen & Coates, 2019; Thomsen et al., 2013; Young et al., 2005). Enceladus plasma is lost from the inner magnetosphere through Vasyliūnas-type reconnection of closed flux tubes occurring on the nightside, with reconnected flux tubes returning to the inner region through the dawn sector. Tailward of the region of returning flux, mainly on the dawn side, lies the Dungey-cycle reconnection line, feeding reconnected lobe flux tubes sunward along the dawn flank. This region should be characterized by hot light solar wind ions. Thomsen et al. (2015) observed the possible plasma signature of Dungey-type lobe reconnection pursuant to a region Vasyliūnas-type reconnection.

In this study, we will examine Saturn's nightside ring current in the context of Saturn's magnetosphere, and how the system responds to internal and external drivers. The two main drivers considered in this paper are external driving by the solar wind and internal driving by the planetary period oscillations (PPOs). We note that e.g. Cowley et al. (2017) and Sorba et al. (2018) previously modelled the variation of Saturn's magnetodisc and current sheet with PPO periods. Our study builds on the comprehensive work of Bradley et al. (2020), who studied the solar wind and magnetospheric conditions during Cassini's F-ring and proximal orbits. They showed that magnetospheric storms involving significant Dungey-cycle reconnection in the tail are triggered during compressions by the solar wind, with "major" compression-responses occurring when the two PPO systems are rotating within ± 90° of antiphase (such times are referred to, for brevity, as “PPO antiphase” throughout this paper). While weaker "minor" compression-responses occur when the two PPO systems are rotating within ± 90° of in phase (termed “PPO in phase” throughout this paper). Here we examine the same proximal orbits as Bradley et al. (2020), focusing on the nightside ring current and its modulation both by changing solar wind conditions and relative PPO phases. We will compare our results with observations of Saturn's dayside/dawn ring current examined by Bunce et al. (2007). For brevity, this paper will be referred to as B2007.

1.2. Planetary Period Oscillations

Despite the near-perfect axisymmetry of Saturn's internal magnetic field (Dougherty et al., 2018), rotating modulations termed PPOs have been observed throughout Saturn's magnetosphere (see review by Carbary & Mitchell, 2013, and papers by Andrews et al., 2011; Hunt et al., 2015; Provan et al., 2019b). These systems give rise to intervals of thickening and thinning of the nightside plasma/current sheet during their rotational cycles, as well as north-south oscillations (Cowley & Provan, 2017; Cowley et al., 2017; Morooka et al., 2009; Provan et al., 2012; Ramer et al., 2017). Bradley et al. (2020) examined how Saturn's magnetosphere responds to solar wind compressions and rarefactions. They found that major compression-response

events were triggered when the magnetosphere was compressed by the solar wind and when the two PPO systems were in antiphase, this PPO configuration giving rise to maximum variations in the thickness of the current sheet (see Section 2). For an in-depth introduction to PPOs, we refer the reader to these papers, and papers referenced therein. Here we briefly summarize the PPO systems. There are two PPO systems, one associated with the northern hemisphere and the other with the southern. In general, the two systems have slightly different periods (Andrews et al., 2010; Gurnett et al., 2009a, 2009b; Kurth et al.,2008; Provan et al., 2011). Both the northern and southern PPO systems are observed in the magnetic field data as quasi-sinusoidal perturbations of a few nT amplitude rotating at the corresponding PPO period about the planetary axis, varying only slowly with radial distance and latitude. Each system produces a quasi-uniform perturbation field in the equatorial region which closes in a rotating quasi-dipolar perturbation field over the corresponding planetary pole (Andrews et al., 2010; Provan et al., 2009, 2011).

The two PPO systems constructively and destructively interfere over the beat cycle of the oscillations, with the beat phase of the two oscillations given by

$$\Delta\Phi = \Phi_N - \Phi_S, \tag{2}$$

where $\Phi_{N,S}$ are the global phases of the northern and southern PPO systems, giving the orientation of each PPO system relative to the noon meridian (see e.g. Andrews et al., 2011).

When the two oscillations are in phase we expect maximum north-south oscillations of the current sheet and minimum thickening and thinning. Conversely when the two oscillations are in antiphase we expect minimum north-south oscillations of the current sheet but maximum thickening and thinning. Magnetic reconnection in the tail is more likely to occur when the current sheet is thinned, and so is favored under PPO antiphase conditions. Jackman et al. () found that plasmoids and travelling compression regions preferentially occurred at PPO phases where the current sheet is thinned and the magnetospheric field lines and plasma are displaced outwards from the planet. Thomsen et al. (2017) reported periodic variation in the thickness of Saturn's nightside plasma sheet. Bradley et al. (2018) conducted a statistical study of in excess of 2000 tail reconnection events. Overall these events again occur preferentially when the two PPO phases are close to antiphase, when the tail current sheet is expected to be locally thinned and threaded by a weakened colatitudinal (B_θ) field.

2. Internal and External Drivers of Magnetospheric Storms During Cassini's Proximal Orbits

Bradley et al. (2020) presented a comprehensive study of the internal (PPOs) and external (solar wind) drivers of magnetospheric storms observed during Cassini's final 44 orbits, comprising the F ring orbits and the proximal orbits studied here. They used propagated solar wind data (Tao et al., 2005), together with Cassini observations of Galactic Cosmic Rays (GCR) and Solar Energetic Particles (SEPs) (Roussos et al., 2018a, 2018b), to determine when solar wind compression events impinged on the Saturn's magnetosphere. They identified nine significant solar wind compressions during the proximal orbits. The majority are associated with corotating interaction regions propagating in the heliosphere, producing ~2–3.5 day intervals of magnetospheric activity that are recurrent with the ~26 day solar rotation period. However, two solar wind compression events were 'unanticipated' and believed to be associated with interplanetary coronal mass ejections (ICMEs).

Bradley et al. (2020) studied Saturn's magnetospheric response to the solar wind compressions, using magnetic field data, low-frequency extensions (LFE) of Saturn's Kilometric Radiation (SKR) (Jackman et al., 2009; Reed et al., 2018) and energetic particle data. SKR LFEs are associated with enhanced field-aligned coupling currents, associated with dynamical events in Saturn's magnetosphere. Such events were first detected via enhancements in SKR power correlated with the solar wind dynamic pressure observed during approach to Saturn by the Voyager spacecraft in 1980/1981 (Desch, 1982; Desch & Rucker, 1983), thus being modulated on ~26 day solar rotation time scales by the structure of the interplanetary medium. Based on the SKR LFEs, Bradley et al. (2020) categorized Saturn's magnetospheric response

to 20 solar wind compressions as either a 'minor' or 'major' compression-response event. Major compression-response events are those with LFEs with durations greater than one planetary/PPO rotation period, while minor compression-response events either have no LFEs or LFEs lasting for less than one planetary period.

Both major and minor compression-response events occur during solar wind compressions, but they tend to occur at different phases of the PPO beat cycle (Bradley et al., 2020). Bradley et al. (2020) found that major compression-response events preferentially occur over the ~180° beat phase sector centered on antiphase conditions when the plasma sheet is thinned, creating optimal conditions for tail reconnection and plasmoid release. Such tail reconnection, and the consequent transport of tenuous energized plasma results in enhanced field-aligned coupling currents, poleward contractions of dawn-brightened aurora and energetic particle precipitation. Hot plasma is accelerated inwards towards Saturn, forming a dipolarization front, and causing the plasma sheet to expand away from the equator planetward of the reconnection region (see also previous studies of plasma injection signatures at Saturn, for example by Mitchell et al., 2009; Kinrade et al., 2020). Bradley et al. (2020) reported several instances during the F ring and proximal Revs when Cassini was inbound in the northern lobe region and became engulfed by such hot plasma (the term "Rev" is an abbreviation of revolution, and refers to an orbit of Cassini around Saturn defined from one apoapsis to the next). The presence of hot plasma causes high-frequency fluctuations in the magnetic field, which are absent in the tail lobes. Following injection episodes observed e.g. on the inbound pass of a given Rev, such particles are retained within the plasma sheet in this region for at least several subsequent planetary rotations during the outbound pass.

Table 1 gives the solar wind and magnetospheric conditions during the proximal Revs, as identified by Bradley et al. (2020) (see, in particular, Figure 12 in that paper where the solar wind and magnetospheric conditions during the F-ring and proximal Revs are summarized). Column 1 gives the Rev number and column 2 the time of periapsis. All times are given in doy2004, convenient for multi-year datasets, defined such that $t = 0$ corresponds to 00:00 UT on January 1, 2004, effectively the start of the Cassini science mission. In column 2, the day and month of periapsis are also given, with the year being 2017 for all proximal Revs. Columns 3 and 4 give the start and stop times of the intervals selected for ring current modelling ($4.25 < r < 14\ R_s$, as will be described in Section 4). Column 5 indicates the prevailing solar wind and magnetospheric conditions, while columns 6 and 7 give the start and stop times of such solar wind conditions. Column 8 describes whether the magnetospheric and solar wind conditions described in columns 5–7 persist for the entire interval selected for ring current analysis, or are just observed pre- or post- periapsis. This is important because the modelled ring current parameters are determined over a ~2-day interval centered on periapsis. We wish to distinguish between intervals when the ring current responds to uniform solar wind and magnetospheric conditions, and intervals when the state of the ring current reflects more variable conditions. In column 5, we also present the solar wind compression event nomenclature devised by Bradley et al. (2020), where the letters in each label identify successive ~26 day solar rotation periods (with A occurring at the start of the F ring orbits), while numbers identify successive events within each solar rotation. Event K1* occurring during Rev 288 is an "unanticipated" event associated with a solar energetic proton event, indicating the approach and impact of an interplanetary shock.

The Revs in Table 1 are categorized and color coded with respect to solar wind conditions and Saturn's magnetospheric response as follows.

Category 1—blue: a Rev associated with very quiet magnetospheric conditions and a prolonged solar wind rarefaction (Revs 275, 282, 286, 290).

Category 2—green: a Rev associated with either quiet or intermediate solar wind and magnetospheric conditions (Revs 271,273, 278,279,281, 283, 284, 287, 291).

Category 3—orange: a Rev associate with a minor compression-response event, occurring when the PPO oscillations are in phase (Revs 272, 285, 292).

Category 4—red: a Rev associated with a major compression-response event, occurring when the PPO oscillations are in antiphase (Revs 274, 276,280, 288,289).

Overall, the results of Bradley et al. (2020) emphasize that Saturn's magnetosphere is modulated by concurrent solar wind conditions and the PPOs. Here we will examine how Saturn's nightside ring current responds to these internal and external drivers.

3. Ring Current Models

3.1. Previous Models

3.1.1. Connerney Ring Current Model

Connerney et al. (1981b, 1983) provided the first detailed modeling of the ring current which supports the magnetodisc field at Saturn, based on an initial application to Jupiter's equatorial current sheet (Connerney et al., 1981a). The magnetic field of the Connerney, Acuña, and Ness model (CAN) model is computed by assuming, a priori, an azimuthally symmetric distribution of current which is confined to an annular disc of uniform thickness, extending from an inner edge at a specified cylindrical radial distance to infinity. The current density J_φ is assumed to be inversely proportional to the cylindrical radial distance ($J_\varphi \propto 1/\rho$). The CAN model was discussed further by Edwards et al. (2001). The model uses a cylindrical co-ordinate system (ρ, φ, z), where ρ is the perpendicular radial distance from the planet's spin/magnetic axis, z is the distance from the equator along the axis positive northwards, and φ is the azimuthal angle around the axis positive in the sense of planetary rotation. The ring current magnetic components are parameterized by a, the inner edge of the current sheet, and D the current sheet half-thickness, with the field components outside of the current sheet given by

$$B_\rho^{\pm}(\rho,z) = \pm\mu_0 I_0 \int_0^\infty \frac{d\lambda}{\lambda} J_0(\rho\lambda) J_0(a\lambda) \sinh(D\lambda) e^{\mp z\lambda}, \tag{3}$$

and

$$B_z^{\pm}(\rho,z) = \mu_0 I_0 \int_0^\infty \frac{d\lambda}{\lambda} J_0(\rho\lambda) J_0(a\lambda) \sinh(D\lambda) e^{\mp z\lambda} \tag{4}$$

For $-D \le z \le$ D, inside the current sheet we then have

$$B_\rho^{i}(\rho,z) = \mu_0 I_0 \int_0^\infty \frac{d\lambda}{\lambda} J_1(\rho\lambda) J_0(a\lambda) \sinh(z\lambda) e^{-D\lambda}, \tag{5}$$

and

$$B_z^{i}(\rho,z) = \mu_0 I_0 \int_0^\infty \frac{d\lambda}{\lambda} J_0(\rho\lambda) J_0(a\lambda) \left(1 - e^{-D\lambda}\cosh(z\lambda)\right). \tag{6}$$

In these expressions, $J_n(x)$ is the Bessel function of the first kind of order n. To find the field of a finite current sheet, extending to an outer radius b, we simply compute the field components with a replaced by b in Equations 3–6 above, and subtract these fields from the above expressions.

The CAN model has been employed in several studies of the structure of Saturn's ring current, usually based on fitting the model to in-situ magnetic field measurements from spacecraft to determine the dimension of the disc and its azimuthal current density (e.g. Bunce & Cowley, 2003; Bunce et al., 2007; Connerney et al.,1983; Giampieri & Dougherty, 2004). Connerney et al. (1983) applied this model to the magnetometer data from the Voyager spacecraft encounters. Saturn's ring current was modeled as extending from 8 to 15.5 R_S in cylindrical radial distance and from −3 to 3 in z with a constant half-thickness. Within this cylindrical block the azimuthal current density varied as I_o/ρ with $I_o = 2.8$ MA/R_s^2. Based on Voyager observations the total current in the disc is ∼10 MA (Connerney et al., 1981b, 1983). Bunce and Cowley (2003) and Giampieri and Dougherty (2004) also applied this model to the earlier Pioneer-11 data, while Bunce et al. (2007) made a first examination of the variation of the current with system size using data from 17 orbits in the first two years of the Cassini mission.

Table 1
The Times of Periapsis, the Selected Ring Current Intervals and the Solar Wind/Magnetospheric Conditions on Each Proximal Rev Included in this Study.

REV	Periapsis *t*/doy2004 Day and month (*y*=2017)	Start RC interval *t* /doy2004	End RC interval *t*/doy2004	SW Condition/ Magnetospheric state	Start SW conditions *t*/doy2004	End SW conditions *t*/doy2004	SW state across periapsis Yes/No
271	4,864.378; 26 April	4,863.357	4,865.397	Rarefaction/ Quiet	4,853	4,864	No, inbound only
272	4,870.821; 2 May	4,869.800	4,871.842	Minor compression -response/ G1	4,866.333	4,869.375	No, inbound only
273	4,877.262; 9 May	4,876.237	4,878.283	Intermediate conditions			
274	4,883.698; 15 May	4,882.679	4,884.718	Major compression -response / H1	4,882.958	4,884.750	Yes
275	4,890.135; 22 May	4,889.111	4,891.152	Rarefaction/ Prolonged quiet	4,886.5	4,893	Yes
276	4,896.601; 28 May	4,895.579	4,897.621	Major compression -response/ H2	4,893.083	4,896.16	No, inbound only
278	4,909.537; 10 June	4,908.514	4,910.556	Rarefaction/ Quiet	4,899	4,908	No, inbound only
279	4,915.997; 16 June	4,914.974	4,917.022	Rarefaction/ Quiet	4,911.5	4,915	No, inbound only
280	4,922.457; 23 June	4,921.436	4,923.475	Major compression -response/ L1	4,920.167	4,923.417	Yes
281	4,928.926; 29 June	4,927.906	4,929.946	Intermediate conditions			
282	4,935.399; 6 July	4,934.378	4,936.417	Rarefaction/ Prolonged quiet	4,934	4,941.5	Yes
283	4,941.867; 12 July	4,940.845	4,942.884	Rarefaction/ Quiet	4,931	4,941.5	No, inbound only
284	4,948.330; 19 July	4,947.308	4,949.347	Intermediate conditions			
285	4,954.791; 25 July	4,953.771	4,955.809	Minor compression event/ J1	4,949.833	4,951.750	No, inbound only
286	4,961.256; 1 August	4,960.235	4,962.276	Rarefaction/ Prolonged quiet	4,958.5	4,967	Yes
287	4,967.724; 7 August	4,966.704	4,968.746	Rarefaction/ Quiet	4,958.5	4,967	No, inbound only
288	4,974.183; 14 August	4,973.167	4,975.199	Major compression -response/ K1*	4,970.6250	4,974.750	Yes
289	4,980.641; 20 August	4,979.623	4,981.662	Major compression -response/ K1	4,979.5417	4,981.708	Yes
290	4,987.096; 27 August	4,986.081	4,988.109	Rarefaction/ Prolonged Quiet	4,985	4,991.5	Yes
291	4,993.551; 2 September	4,992.537	4,994.569	Intermediate conditions	4,985	4,991.5	No, inbound only
292	5,000.007; 9 September	4,998.988	5,001.027	Minor compression -response /L1	4,997.0,833	4,999.4583	No, inbound only

Each rev is color-coded according to the solar wind/magnetospheric conditions as described in the text.

3.1.2. Carbary Model

Another method of modelling Saturn's ring current was presented by Carbary et al. (2012) and Carbary (2019), with Carbary's (2019) model of Saturn's ring current for local midnight presented here in Figure 2a, where the azimuthal current density is color coded as shown on the right. The data are plotted in the ρ/z plane, symmetrical about the equatorial plane. Carbary (2019) constructed the model directly from magnetometer observations, selecting magnetic field measurements from Saturn Orbit Insertion (SOI) in 2004–2016. These data were first binned in cylindrical co-ordinates to obtain a continuous estimate of the mean magnetic field. The azimuthal current density was then determined from the curl of the field using

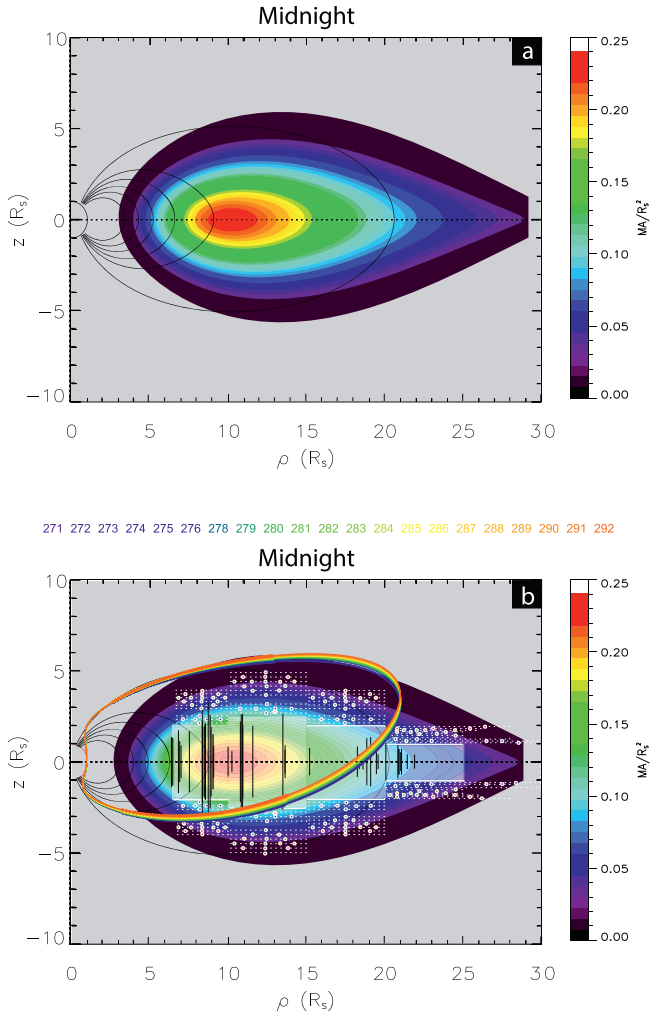

Figure 2. (a) and (b) Carbary's (2020) model of Saturn's ring current for local midnight, where the azimuthal current density is color coded as shown on the right. The data are plotted in the ρ/z plane, symmetrical about the equatorial plane. Overplotted in (b) as semi-transparent white blocks is the initial ring-current model for the proximal Revs. The model consists of 4 blocks with widths of 6.5–10, 10–15,15–20, and 20–25 R_s, and half-thickness of 2, 2.5, 2, and 1 R_s, respectively. The thickness of the ring current and the radial position of its outer boundary are then determined on a Rev-by-Rev basis. The dashed white lines show the dimensions of the resulting best-fit ring current model for the individual Revs, as also indicated by the colored circles with white edges. The Revs have been color coded by their category, defined according to solar wind and magnetospheric conditions determined by Bradley et al. (2020). Also shown in (b) are the trajectories of the 21 proximal Revs used in this study, Rev 271-291 but excluding Rev 277, plotted in the ρ/z plane. Both the trajectories of the spacecraft and our current model are plotted with respect to the warped magnetodisc of the Arridge current bowl (2008). The 47 solid black vertical lines are the thickness measurements of Saturn's nightside ring current observed by Staniland et al. (2020).

Maxwell's equations. Finally, an analytical model was fitted to current density values which included both a local time variation of the current's median strength and location, and a radial variation of its width. The model results show that the ring current has a teardrop shaped cross section rather than a rectangular cross section employed by the early models (Connerney et al., 1983). The outer cusp-end of the teardrop-shape extends to ~20 R_s on the dayside and to ~25 R_s on the nightside. The inner blunt end of the teardrop is located near 5 R_s at all local times. The maximum current density occurs at ~10 R_s at all local times. However, the ring current has a strong local time dependence, with a maximum current density observed at ~1 h LT and a minimum at ~16 h LT. Figure 2b provides an example of the model employed here (introduced in Section 3.2) and a comparison with the Carbary model which will be discussed in Section 6.1. We also show the trajectory of the proximal Revs in the ρ/z plane, as introduced in Section 4.1.

3.2. Our Model

Considering the knowledge gained from the ring current models described above, we commence by assuming an axisymmetric equatorial current sheet, based on that described by Connerney et al. (1981b, 1983). Considering next the cross-sectional shape of the ring current, we approximate a teardrop shape using four CAN current discs, each of finite width and constant thickness, as exemplified by the four grey boxes over-plotted in Figure 2b. The current density is again taken to be $\boldsymbol{j}(\rho) = (I_0 / \rho)\hat{\boldsymbol{\varphi}}$, where parameter $\mu_0 I_0$ is identical in all four CAN discs, so that the current density is continuous across the boundaries of each of the four discs. The total current in each disc is then directly modulated by its half-thickness, with a constant ratio between each disc.

We assume that the ring current is centered on Saturn's seasonally warped magnetic equatorial plane, described by Arridge et al. (2008b). They modeled the distance from the planetary equatorial plane to the current sheet, measured along a direction parallel to Saturn's spin axis, as

$$Z_{cs} = \left(-\tan\theta_{SUN}\right)\tanh\left(\frac{\rho}{R_H}\right) \tag{7}$$

where ρ is the cylindrical radial distance and R_H is the hinging distance, the characteristic radial distance at which the warped magnetic equatorial plane departs from the planetary equatorial plane towards the direction of the solar wind flow θ_{SUN} (taken to be the negative of the subsolar latitude). During the near-northern summer solstice conditions that prevailed during the proximal orbits, θ_{SUN} had the near-constant value ~−27°, such that the current sheet center beyond ~R_H was displaced southward of the planetary equator, as depicted in Figure 1. We note that the value of R_H, typically observed in the range between 16 and 35 R_s, will vary with the dynamic pressure of the solar wind flow, becoming smaller as the dynamic pressure increases.

The expressions for the magnetic field of a curved current sheet are given by Pensionerov et al. (2019) as follows:

$$\left(\mathbf{B}_{\text{curv}}\right)_{\rho} = B_{\rho}(\rho, z - z_{cs}(\rho)) \tag{8}$$

$$\left(\mathbf{B}_{\text{curv}}\right)_{z} = B_{z}(\rho, z - z_{cs}(\rho)) + \frac{\partial z_{cs}(\rho)}{\partial \rho} B_{\rho}(\rho, z - z_{cs}(\rho)) \tag{9}$$

where the second term on the right side of Equation 9 is such that overall the field is exactly divergence-free.

To model the magnetic field observed on the proximal orbits, we also need to account for the magnetic signature of other external field sources, specifically the magnetopause-tail current systems. Following the results of Alexeev and Feldstein (2001) and Alexeev and Belenkaya (2005), B2007 assumed the presence of a north-south fringing field B_z near the equatorial plane that varies linearly with distance away from the Sun. The value of this fringing field varied from a few nT negative near the subsolar magnetopause, due to the compressive effect of the solar wind dynamic pressure, to a few nT positive at similar distances on the nightside, due to the effect of the tail currents. Kellett et al. (2009) considered a similar linear dependence of B_z, while also introducing a related B_x field which ensures that the fringing field in the middle magnetosphere is curl free. The same model as Kellett et al. (2009) is adopted here, given by x and z KGS components such that within distances of several R_s of the equatorial plane

$$B_z(x) = -a(x - x_0) \tag{10}$$

and

$$B_x(z) = -az. \tag{11}$$

where a is the parameter defining the linear gradients of these fields. The B_x field is taken to be zero on the planetary equator, while the B_z field passes through zero at $x = x_0$.

Our ring current model employs four CAN discs, the inner three of which lie between fixed cylindrical radial ranges of 6.5–10, 10–15, and 15–20 R_s, while the fourth lies between 20 R_s and an outer radius R_2 that is determined as a fit parameter. As we are observing the nightside ring current, this outer radius is not constrained by the position of the magnetopause boundary. From the inner to the outer disc, the "baseline" half-thicknesses of the discs are taken to be $D = 2$, 2.5, 2, and 1 R_s, thus, approximating a "teardrop" shape. For each rev, the thickness of the four discs are fixed in ratio, and are varied by the thickness scaling factor k_D to determine the optimal fit to the data. k_D is then the second ring current fit parameter. The third ring current fit parameter is the current density, $\mu_0 I_0$, which together with the fringing field parameters a and x_0 and the magnetic equatorial hinging distance $R_{H,}$ complete the set of six model fit parameters. For each Cassini Rev, the fit parameters are determined by a least squares fitting process described in Section 4.3. The fitting procedure is performed simultaneously for all four CAN current discs, with the current density parameter being constant across all four discs, so that there is no jump in current density at the interfaces between the discs.

Our baseline ring current model is shown in Figure 2b as shaded white blocks, overplotted on the Carbary (2019) ring current model for the midnight meridian. When plotting our current sheet model we define $z = 0$ R_s as the center of the warped current sheet (Arridge et al., 2008), with the modeled ring current extending symmetrically either side. We note that the Carbary (2019) ring current model was centered on Saturn's equatorial plane. However, this model was based on magnetic field measurements averaged between July 2004 and 2016, so over nearly half a Saturn year, from shortly after southern summer solstice when $\theta_{\text{SUN}} \sim 24°$, to approximately northern hemisphere solstice when $\theta_{\text{SUN}} \sim -26°$. The center of the warped current sheet position averaged over this interval should be approximately located with the planetary equatorial plane.

Having determined the best fit parameters for a given Rev, we can then obtain other quantities of interest as follows. Denoting the inner and outer cylindrical radii of disc n by $R_{1,n}$ and $R_{2,n}$, with half thickness D_n, the total current in the ring current carried by all four discs is given by

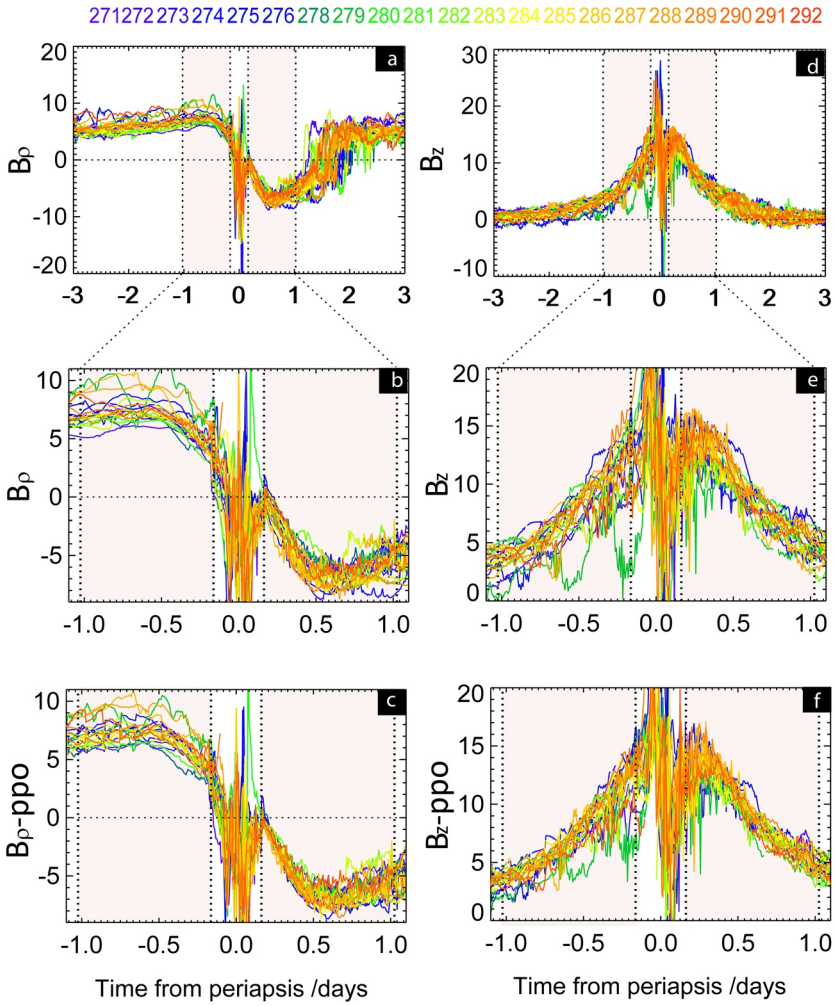

Figure 3. (a) and (d) show superposed plots of the B_ρ and B_z components of the residual magnetic field for Revs 271 to 292, color-coded on a Rev-by-Rev basis. The data are plotted with respect to time, labelled in days, where t=0 is the time of periapsis. We show data from 3 days before periapsis to 3 days after. The data are presented at a resolution of 10 min. The four dashed vertical lines denote the two regions where $4.25 < r < 14\ R_s$, inbound and outbound, corresponding to the radial ranges where data was selected for fitting of the ring current model. These two regions are shown with a pink background. (b) and (e) presents the same data as in (a) and (d), focusing in on the main ring current signature by only presenting data over a time range covering 1.1 days either side of periapsis. (c) and (f) presents the same data as in (b) and (e) but with the PPO signatures removed.

$$I_T = 2I_0 \sum_{n=1}^{n=4} D_n \ln\left(\frac{R_{2,n}}{R_{1,n}}\right) \tag{12}$$

The mean half-width of the ring current, $\bar{D}$, is defined as the mean value over the contributing current discs weighted by their contribution to the total current

$$\bar{D} = \sum_{n=1}^{n=4} 2I_0 D_n^2 \ln\left(\frac{R_{2,n}}{R_{1,n}}\right) / I_T. \tag{13}$$

The ratio of the magnetic moment of the ring current to the magnetic moment of the planetary dipole, is also calculated as

Table 2
The Best-Fit Ring-Current and Fringing-Field Parameters for Each Proximal Rev as Presented in Figure 8.

Rev	$\mu_0 I_0$ /nT	k_D	$\overline{D}$ /R_s	R_2 /R_s	IT /MA	k_{rc}	R_H /R_s	a /nT R_s^{-1}	x_0 /R_s	RMS (nT)
271	32	1.8	3.86	23	14.32	0.72	35.0	0.20	-9	0.80
272	37	1.7	3.58	25	16.14	0.92	22.5	0.20	-10	0.78
273	36	1.8	3.76	26	16.87	1.02	35.0	0.35	-11	1.18
274	38	1.9	4.00	25	18.53	1.05	35.0	0.25	-14	1.30
275	52	1.3	2.68	28	18.08	1.23	35.0	0.10	-7	0.98
276	53	1.2	2.57	23	15.81	0.79	30.0	0.10	-11	1.73
278	45	1.2	2.37	36	15.75	1.58	35.0	0.05	-1	0.89
279	35	1.7	3.58	25	15.27	0.87	30.0	0.30	-10	1.11
280	36	2.0	4.12	28	19.26	1.30	25.0	0.50	-16	2.13
281	39	1.7	3.58	25	17.01	0.96	35.0	0.24	-12	1.02
282	51	1.1	2.20	33	15.89	1.39	35.0	0.10	-3	0.75
283	33	1.8	3.79	25	15.24	0.86	35.0	0.25	-10	1.14
284	35	1.8	3.82	24	15.92	0.85	27.5	0.30	-11	1.19
285	41	1.6	3.40	24	16.58	0.88	35.0	0.25	-10	1.16
286	49	1.2	2.51	26	15.31	0.92	35.0	0.20	-6	1.17
287	43	1.6	3.40	24	17.38	0.92	35.0	0.25	-10	1.01
288	42	1.9	4.00	25	20.48	1.16	30.0	0.40	-15	1.49
289	44	1.9	3.97	26	21.77	1.31	35.0	0.35	-17	1.27
290	55	1.2	2.55	24	16.68	0.89	30.0	0.15	-9	1.61
291	43	1.5	3.16	25	16.55	0.94	35.0	0.20	-9	1.03
292	38	1.8	3.76	26	17.81	1.07	27.5	0.35	-14	1.19

Also shown are the RMS values between the best-fit model and the data.

$$k_{RC} = \frac{I_o^2 \mu_0}{2 B_P R_p^3} \sum_{n=1}^{n=4} D_n^2 \ln\left(\frac{R_{2,n}}{R_{1,n}}\right) \times \left(R_{2,n} - R_{1,n}\right) / I_T, \quad (14)$$

where B_p is the planetary dipole field at the magnetic equator, $R_1 = 6.5\ R_s$ and $R_p = R_s = 60{,}268$ km and $B_p = 21{,}140.2$ nT, approximate to the Cassini internal field model of Dougherty et al. (2018).

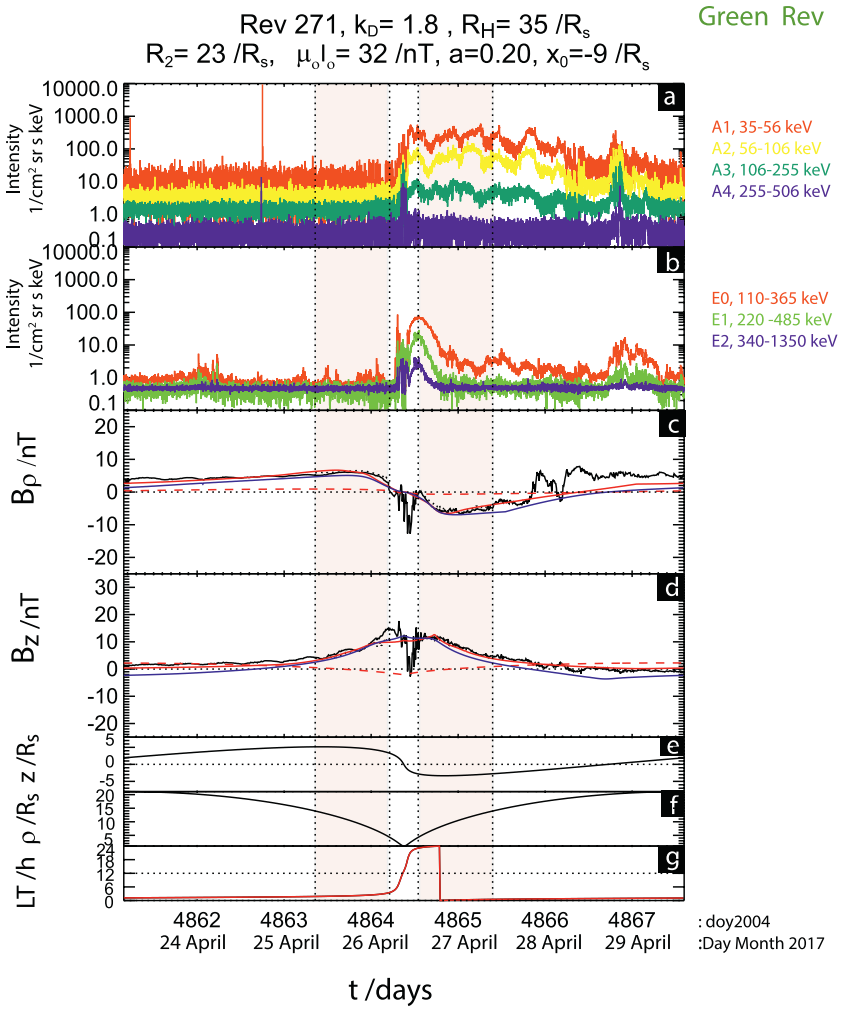

Figure 4. Data from Rev 271. (a) presents color-coded ion intensities from LEMMS channels A1-A4 spanning 35-606 keV for dominant protons as indicated on the right of the panel (see Roussos et al., 2018a, 2018b; Bradley et al., 2020, for more details). (b) similarly shows color-coded electron intensities for LEMMS channels E0-E2 spanning 110-1350 keV as also indicated on the right. (c) and (d) present the B_ρ and B_z components of the residual magnetic field, in cylindrical polar co-ordinates referenced to Saturn's spin/magnetic axis. These data are presented with 10 min resolution. The overplotted solid red lines are the sum of the best-fit ring current and fringing field models, with the dashed red lines showing the fringing field only. The parameters for this best-fit model are presented at the top of the plot. The solid blue lines in show the best-fit model from the analysis of C2020. (e) and (f) then show the position of Cassini in cylindrical coordinates (ρ, z). (g) shows the local time (LT) of Cassini. Overplotted in Figure 4 are four vertical black dotted lines marking r=4.25–14 R_s, both inbound and outbound. These two regions are shown with a pink background. In these regions the black dotted lines shown in (c) and (d) are the PPOs subtracted magnetic field data.

4. Method

4.1. Cassini's Proximal Trajectories

Cassini's final proximal Revs, 271-293, started on April 23, 2017 (day 4861 in doy2004) and ended in Saturn's atmosphere on September 15, 2017 (day 5006 in doy2004). Here we include data from 21 of these Revs. The Cassini mission ended during Rev 293, thus, this partial Rev is not included in the study. Rev 277 is also excluded due to prolonged data gaps within the ring current region. The trajectories of these 21 Revs are over-plotted in Figure 2b, color coded by Rev numbers as shown on the top of the figure. The trajectories are shown in cylindrical coordinates, where ρ is the perpendicular distance from the Saturn's spin (and magnetic) axis. For the trajectories, z is the distance northward from the center of Saturn's current sheet as defined by Equation 7 (Arridge et al., 2008) for $R_H = 32.5\ R_s$, the mean hinging distance found in this study (see Section 5).

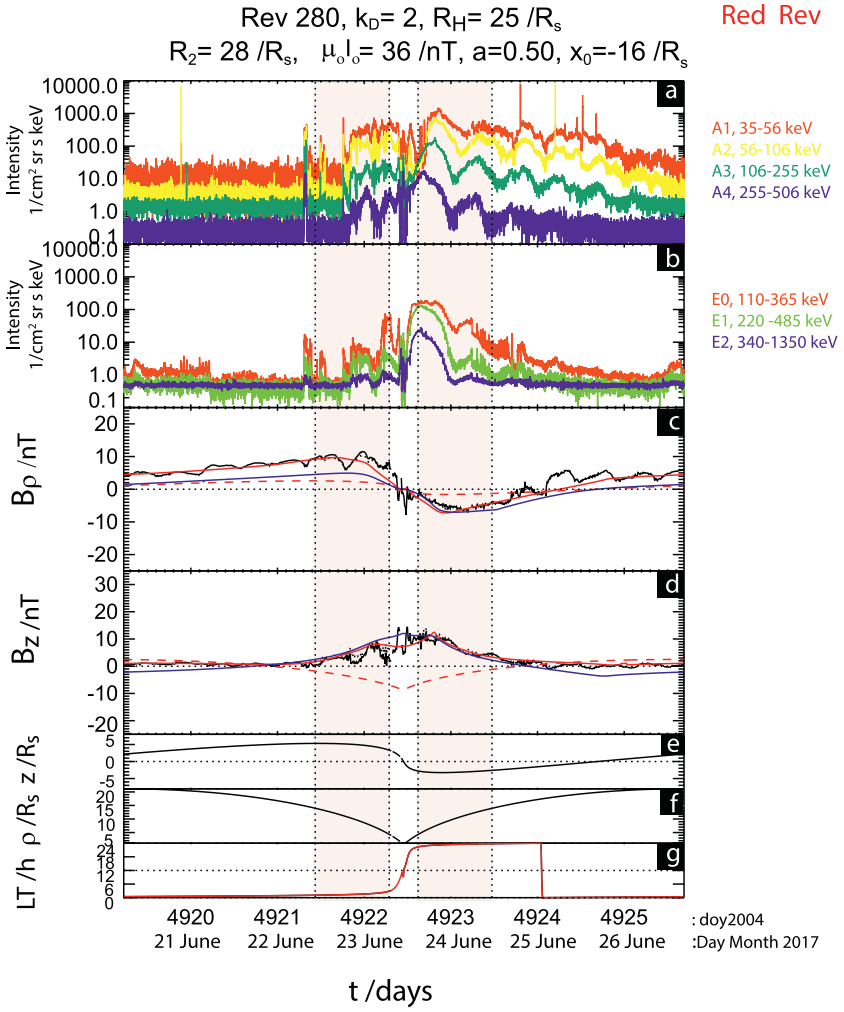

Figure 5. Data plot for Rev 280, in the same format as Figure 4.

Table 3
The Mean and Standard Deviation of All the Categorized Parameters Presented in Figures 7, 9, 10, 11 and 12.

Category / Parameter	Category 1 Mean	1 SD	Category 2 Mean	2 SD	Category 3 Mean	3 SD	Category 4 Mean	4 SD	All Mean	All SD
$\mu_0 I_0$ /nT	51.8	2.5	37.8	4.8	38.7	2.1	40.0	3.7	41.8	6.9
k_D	1.20	0.08	1.66	0.20	1.79	0.10	1.93	0.05	1.60	0.28
R_2 /R_s	27.8	3.9	25.9	3.9	25.0	1.0	26.0	1.4	26.0	3.1
R_h /R_s	33.8	2.5	33.6	2.8	28.3	6.3	31.3	4.8	32.3	3.9
D /R_s	2.48	0.20	3.47	0.47	3.57	0.18	4.02	0.07	3.36	0.62
I_T /MA	16.49	1.20	16.03	1.00	16.84	0.87	20.01	1.42	16.98	1.83
k_{rc}	1.11	0.24	0.97	0.25	0.96	0.10	1.21	0.13	1.03	0.22
α/nT R_s^{-1}	0.14	0.05	0.24	0.09	0.27	0.08	0.38	0.10	0.24	0.11
$x0$/Rs	-6.25	2.5	-9.00	3.38	-11.25	1.89	-15.50	1.29	-10.23	3.91
ΔΦ/deg	151	84	352	86	335	29	200	53	326	127
P_{DYN} /nPa	0.013	0.008	0.009	0.008	0.041	0.029	0.045	0.02	0.022	0.020
R_m /R_s	26.16	4.75	27.41	3.96	20.25	2.65	19.45	1.51	28.8	7.9
A1 / 1/cm² sr s keV	41.1	9.6	253.1	137.9	144.8	106.5	759.8	190.0	295.8	279.9
E0 / 1/cm² sr s keV	5.8	4.7	11.5	12.5	25.4	20.1	49.7	39.1	20.13	24.9

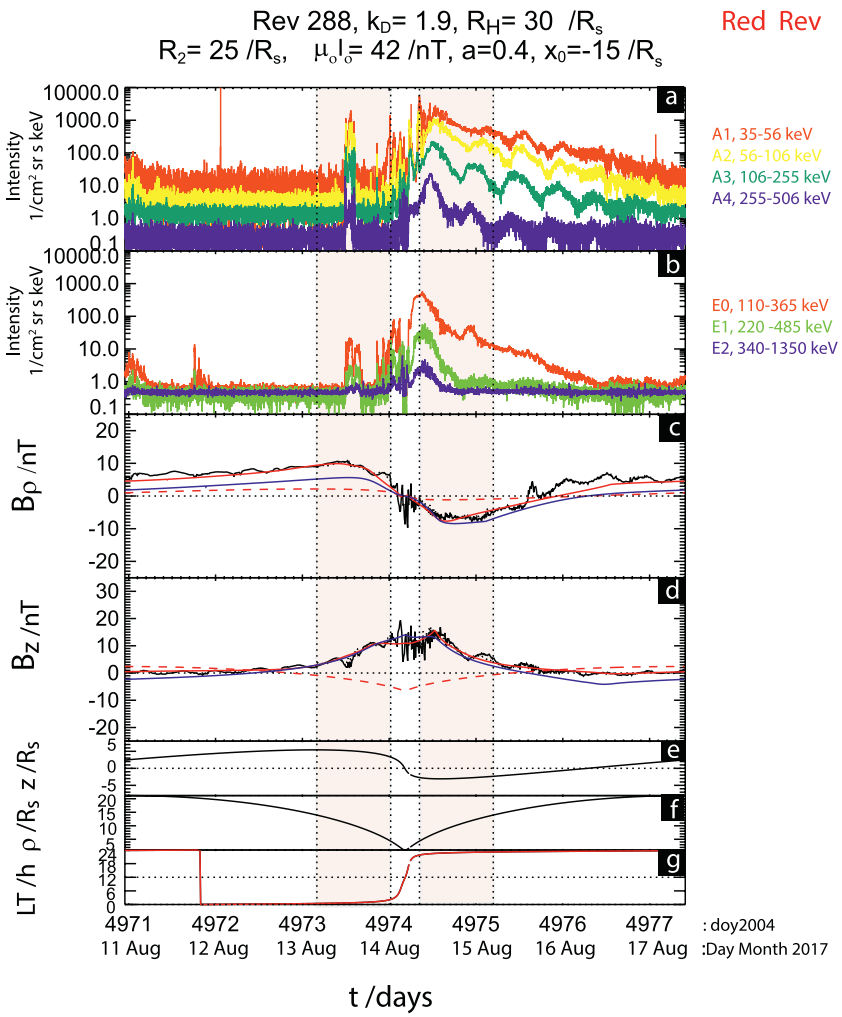

Figure 6. Data plot for Rev 288, in the same format as Figure 4.

The proximal Revs are well suited for studying the nightside ring current, traversing the nightside tail to distances of ~21 R_s in the midnight to post-midnight sector. The trajectories are inclined at an angle of ~61.8° to the equatorial plane, and pass inbound from apoapsis through the plasma sheet/northern tail lobe regions, through a close periapsis on the dayside between the planet's upper atmosphere and the inner edge of the D ring, and then outbound through the southern and central plasma sheet region. Due to the displacement of Cassini northward of Saturn's equatorial plane at apoapsis, combined with the southward seasonal displacement of the plasma/current sheet, in all cases Cassini is expected to be located closer to the center of the plasma sheet on its southern outbound pass than on its northern inbound pass.

There is a change in LT of apoapsis during the proximal Revs, being at ~2 h LT for Rev 271, then shifting over successive orbits to ~23 h LT for Rev 292. The orbital period of the Revs is ~6.7 days, thus corresponding closely to one quarter of the effective solar rotation period at Saturn of ~26 days. Overall, the proximal Revs are all very similar, such that the pass-to-pass differences in the data relate principally to temporal variations in the magnetospheric system associated with dynamics, rather than changes in orbital coverage.

4.2. Magnetic Field Observations

Analysis of the Cassini magnetic field data proceeds as follows. We first remove the 11th-order internal magnetic field model of Dougherty et al. (2018), leaving only the residual magnetic field. In Figures 3a and 3d, we provide superposed plots of the residual B_ρ and B_z components, respectively, for Revs 271–292 (Rev 277 omit-

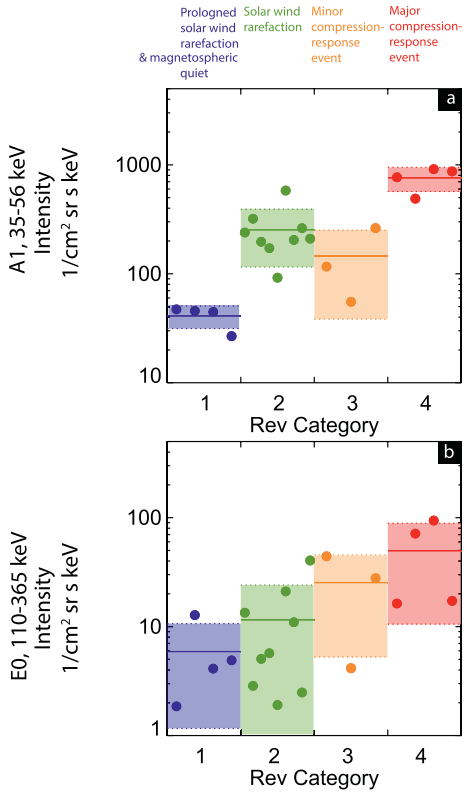

Figure 7. (a) and (b)Box plots showing the mean and standard deviations of the LEMMS proton intensity for the ion energy channel A1 and the electron intensity for energy channel E0. The mean values are determined for observations made between $r = 4.25$–$14\ R_s$ when Cassini traverses through the plasma sheet on its outbound trajectory. The colored circles give the values from the individual Revs, color-coded by Rev category. For each of the Rev categories 1–4, the solid lines give the mean intensity values and the shaded regions bound by two dashed lines give their standard deviation. The box plots are color coded-according to the Rev category.

ted), color-coded on a Rev-by-Rev basis. The data are plotted with 10 min resolution to allow the large-scale features to be clearly observed, and are shown from 3 days before to 3 days after periapsis, which corresponds to $t = 0$ in these plots. These plots thus encompass nearly all of the field data from each ~6.7 day Revs, omitting only a small interval near to apoapsis in each case. The residual field is due to Saturn's ring current, the magnetopause and magnetotail fringing fields, and the two PPO systems. In the inner and middle magnetosphere, field perturbations due to the ring current are by far the most influential, with the magnetopause and magnetotail fringing fields being typically ~10% of the main perturbation fields in these regions (e.g. Bunce et al. 2007). Close to periapsis there are additional signatures due to the intra-D ring current and possible ionospheric currents (Cao et al., 2020; Khurana et al., 2018; Provan et al., 2019a). These signatures are excluded from this ring current analysis by including only data observed at radial distances exceeding 4.25 R_s. The averaged times of this region are marked by the inner pair of vertical dotted lines in the panels of Figure 3, resulting in the exclusion of the central ~8 h of magnetic field data.

Figure 3 shows that apart from the excluded large fluctuating fields in the region near periapsis, consistent perturbations principally associated with the ring current are present from pass to pass. These ring current perturbations would not be significantly changed if we had employed another recent model, for example, Cao et al. (2020). The B_ρ perturbations in Figure 3a switch sign across periapsis from peak positive values ~8 nT inbound in the northern region to similar peak negative values outbound in the southern region. They then reverse sign again more sharply across the nightside current sheet on the outbound pass, the inbound-outbound asymmetry again being due to the northward displacement of apoapsis combined with the seasonal southward displacement of the current sheet center. Values of B_ρ near apoapsis are reduced to ~5 nT. The B_z perturbations in Figures 3d and 3e show peak positive values ~15 nT near the planet, falling more rapidly to small, few nT, but still on average positive values near to apoapsis.

As can be seen from the trajectory plotted in Figure 2b, Cassini passes obliquely through the tail plasma/current sheet in the southern hemisphere when moving outbound from the planet. This results in highly variable fluctuations in the perturbation B_ρ component being observed on the outbound passes, visible in Figure 3a, which Cassini starts to observe about ~1.2 days after periapsis. In order to omit these fluctuating signatures from our analysis we have also excluded all observations beyond $r > 14\ R_s$, the averaged times for which are shown by the outer pair of dashed vertical lines in the panels of Figure 3. The data to be modeled in our study are therefore those lying between the pairs of dashed vertical lines in Figure 3, shown against a pink background. They cover about 1 day either side of periapsis, and contain the largest and principal variations of the fields concerned. In Figures 3b and 3e, we show the same data as in Figures 3a and 3d but focusing in on the field data modeled in this study. Although, as indicated above, the overall ring current signatures are very repeatable on a Rev-by-Rev basis, there is a spread of a few nT between the magnetic fields observed on different Revs. This is in part due to the northern and southern system PPO fields, which we thus remove.

Provan et al. (2019b) described the phases and amplitudes of the northern and southern PPO oscillations along the proximal orbit trajectories. The few-nT amplitudes of the northern oscillations are generally larger than those of southern oscillations during northern hemisphere summer, with the amplitude ratio k (northern amplitude/southern amplitude) being ~1.3 during the proximal orbits (Provan et al., 2018). Using these results, we have determined empirical models of the northern and southern PPO oscillations along the proximal trajectories, and have subtracted the two PPO oscillation model values from the proximal data set. The results are presented in Figures 3c and 3f, which show the same interval as in Figures 3b and 3e but with the PPO signatures removed.

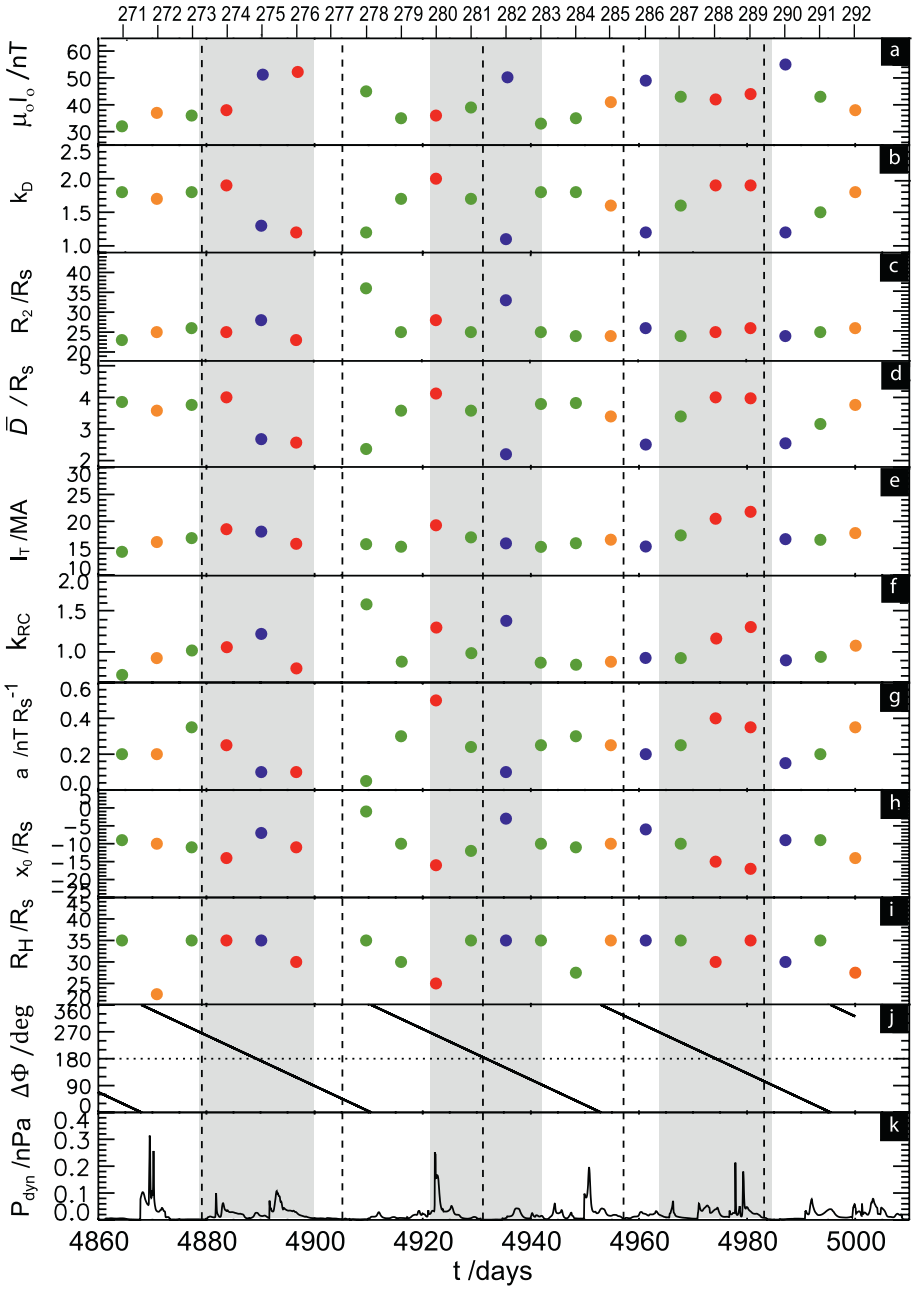

Figures 8. (a)–(i)present a summary of the best-fit ring current and fringing field parameters determined on a Rev-by-Rev basis for all full proximal Revs, 271-292. For each Rev, the parameters are plotted at the time of periapsis, which is also labelled at the top of the figure. (a)-(c) present a summary of three best-fit ring current parameters, $\mu_0 I_0$, describing the magnitude of the current density in the ring current, k_D, the ring current thickness scaling parameter and R_2, the outer boundary of the ring current. (d)-(f) present three additional ring current parameters $\bar{D}$, the mean half thickness of the ring current, I_T, the total current in the ring current and k_{RC} the ratio of the magnetic moment of the ring current to the magnetic moment of the planetary dipole. (g) and (h) present the two parameters relating to the magnetopause and magnetotail fringing fields, a, the gradient of the fringing field and x_0 the distance at which the magnetopause and magnetotail currents are equal, respectively. (i) presents R_H, the hinging distance of the Arridge bowl. The Revs have been classified into four separate categories according to solar wind and magnetospheric conditions determined by Bradley et al. (2020), with each category color coded as throughout this paper. (j) presents the PPO beat phase. (k) shows the solar wind dynamic pressure propagated to Saturn using an MHD code initialized using data obtained near ~1 AU (Tao et al., 2005). The vertical dashed lines mark the approximate times of cyclical minimia in the galactice cosmic ray flux.

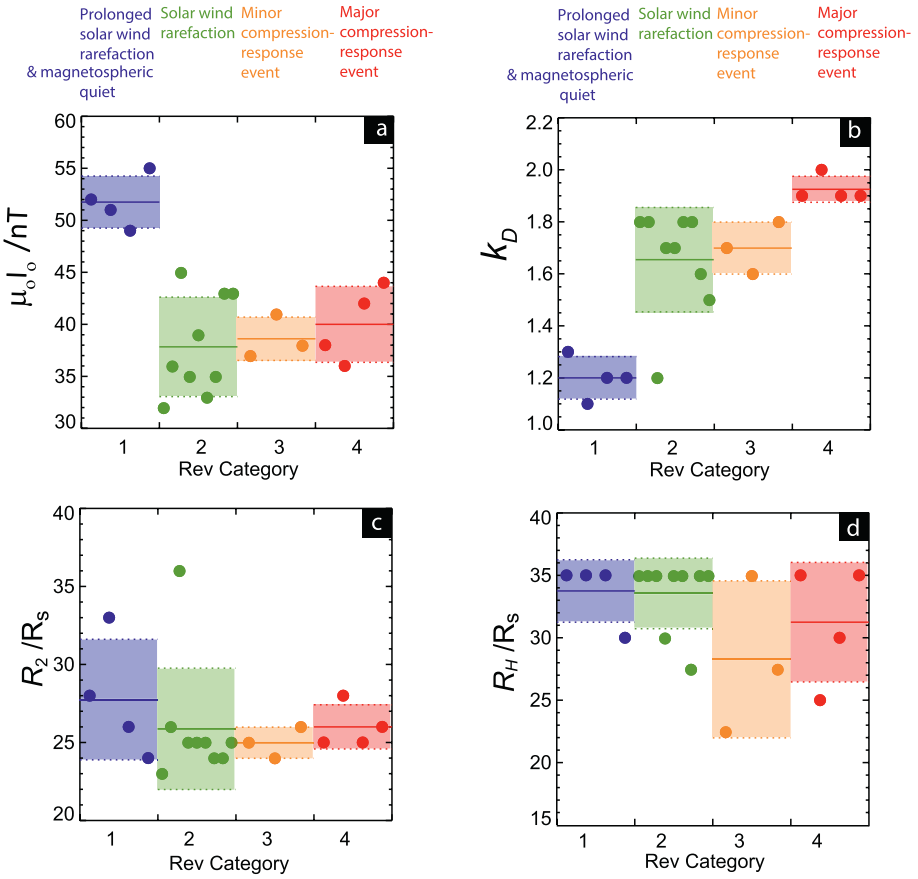

Figure 9. Box plots showing the mean and standard deviations for $\mu_0 I_0$, k_D, R_2, and R_H for the four Rev categories 1–4, shown in the same format as Figure 7.

Since the PPOs only have an amplitude of a few of nT, removing them does not make a huge difference to the overall magnetic field, but it is nevertheless clear that the Rev-to-Rev variation in the residual field values is somewhat reduced both inbound and outbound.

4.3. Fitting the Field Model

As indicated in Section 3.2, the field model employed here has six adjustable parameters, three for the RC model (current density parameter $\mu_0 I_0$, thickness scaling parameter k_D, and outer radius R_2), two for the fringing field (field gradient a and B_z zero position x_0), and the current sheet hinging distance R_H. These are determined for each Rev through an iterative procedure that seeks to minimize the RMS deviation between the model and the data. The RMS deviation between the data and the model is calculated from the squared lengths of the field difference vectors in the ρ-z plane

$$\mathrm{RMS} = \frac{\sqrt{\left(\sum_{i=0}^{i=n}\left(\Delta B_{\rho i}^2 + \Delta B_{zi}^2\right)\right)}}{n} \tag{15}$$

The fitting has four main steps, as follows:

In Step 1, the field on each pass is modeled using a single CAN disc to represent the ring current, with inner edge $R_1 = 6.5\ R_s$, outer edge $R_2 = 25\ R_s$, half-thickness $D = 2.5\ R_s$, and $R_H = 18\ R_s$. The model is fitted to the data to determine the best values of $\mu_0 I_0$, a and x_0. In Step 2, the four-disc ring current model is introduced as described in Section 3.2, but with a fixed outer radius $R_2 = 25\ R_s$ together with $R_H = 18\ R_s$ as in Step 1, and with fringing field gradient a also equal to the best-fit value from Step 1. This model is then employed to iteratively determine best-fit values for current parameter $\mu_0 I_0$ (with an ultimate resolution of 1 nT), thickness scale parameter k_D (resolution

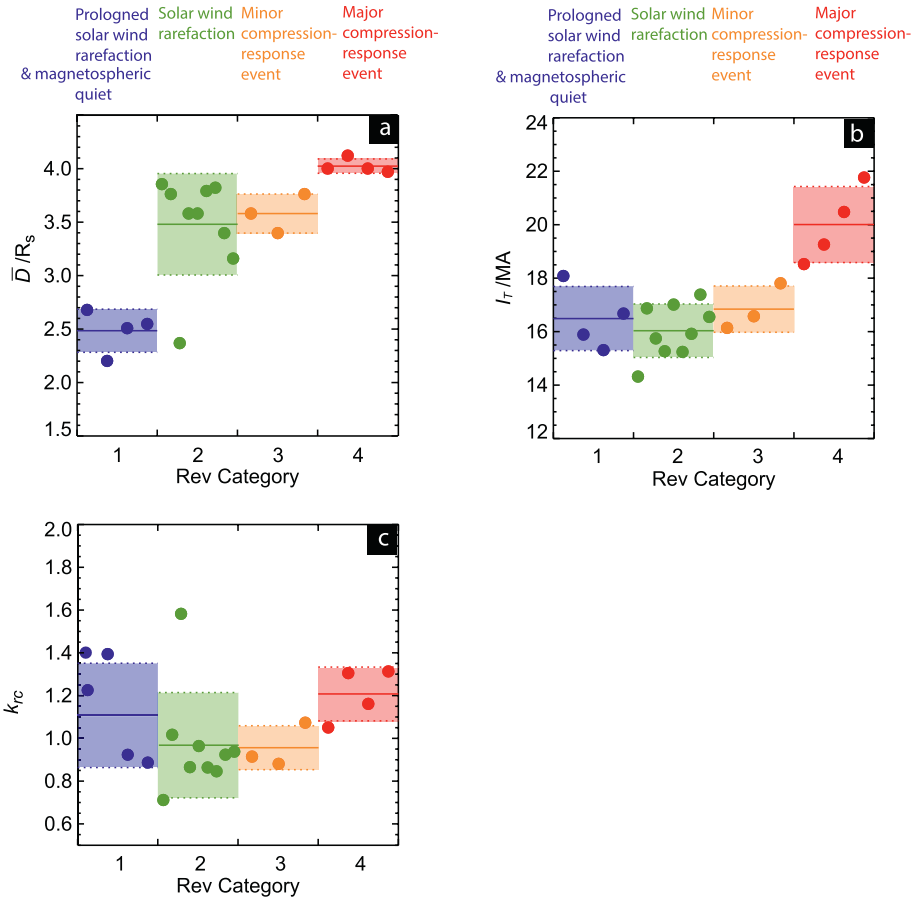

Figures 10. (a)–(c) Box plots of the three parameters derived from the fitted ring current parameter, shown in the same format as Figure 7, showing the mean ring current thickness $\overline{D}$, the total current I_T and and k_{RC}, the ratio of the ring current magnetic moment relative to the magnetic moment of Saturn's dipole field, respectively.

0.1), and fringing field parameter x_0 (resolution 1 R_s). We fit the current density and thickness scale parameters prior to fitting the outer edge of the ring current, as it may be more difficult to discern the signature of the outer edge of the ring current on these proximal revs where we only select data within 14 R_s for analysis. In Step 3, we again run the four-disc ring current model as introduced in Step 2. Here a is initially equal to the best-fit value from Step 1, and k_D, $\mu_0 I_0$ and x_0 equal to the best-fit values determined in Step 2. The model is then employed to iteratively determine best-fit values of R_2 (resolution 3 R_s) and R_H (quantized at 20, 22.5, 25, 27.5, 30, and 35 R_s). We also determine a higher resolution best-fit a, using the a value determined in Step 1 and iterating at a resolution of 0.05 nT R_s^{-1}. In Step 4 we again run the four disc current model introduced in Step 2, k_D, $\mu_0 I_0$, and x_0 are equal to the best-fit values determined in Step 2, and R_H and a are equal to the best-fit values determined in Step 3. Initially using the R_2 parameter determined in Step 3, we run the fitting procedure again to determine a better-fit R_2 value at a resolution of 1 R_s.

5. Results

The best-fit modeled parameters are presented in Table 2. As described in Section 2 and tabulated in Table 1, the Revs have been classified into four separate color-coded categories according to solar wind and magnetospheric conditions determined by Bradley et al. (2020), as summarized in Figure 12 of that paper. The results in Table 2, and throughout this paper, are color coded in the same manner as in Table 1. First, we present the model fitted for three individual Revs, to examine how the model captures the ring current observed under varying solar wind conditions. In Section 5.3, we present an overview of the best-fit field model parameters. Finally, we summarize the LEMMS proton and electron observations.

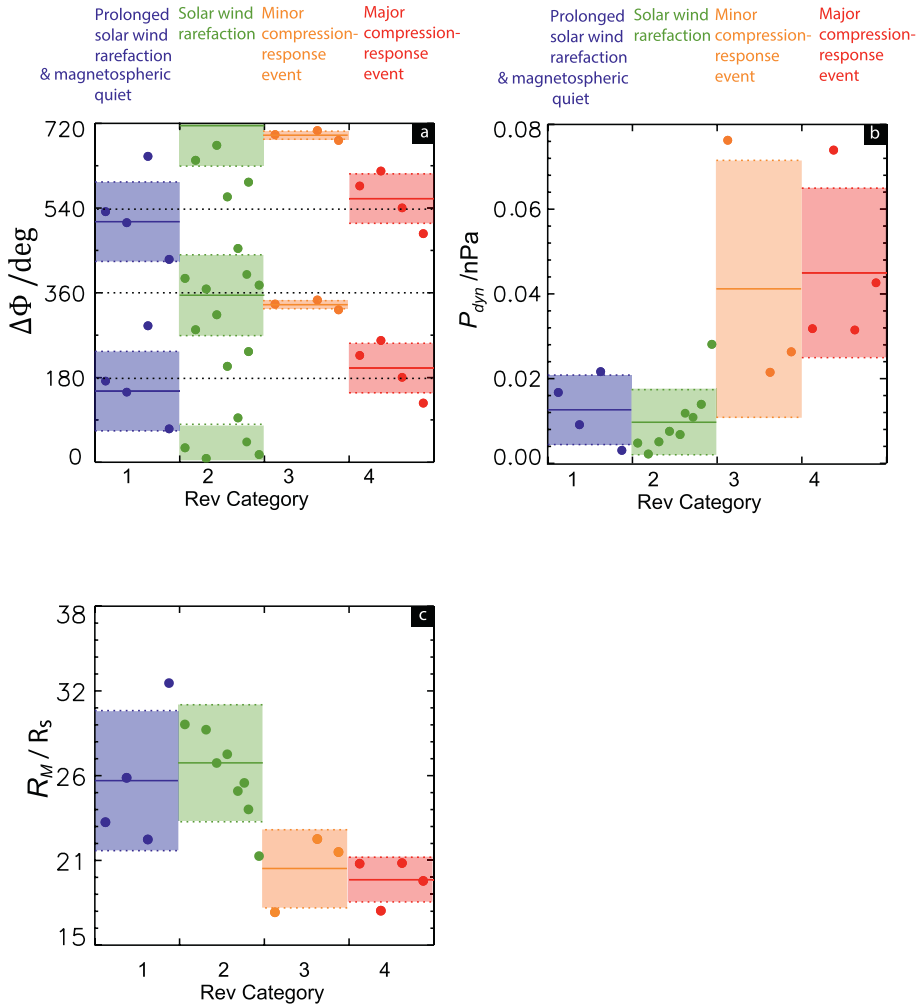

Figure 11. (a) and (b) Box plots of two parameters which can "drive" Saturn's magnetosphere, shown in the same format as Figure 7. (a) presents the mean and standard deviation of the PPO beat-phase for the four Rev categories, and the individual Rev values. (b) similarly shows the propagated solar wind density (Tao et al., 2005), with the mean density calculated on a Rev-by-Rev basis over a time interval spanning 1.5 days either side of periapsis. (c) presents the magnetopause stand-off distance, R_M, calculated using the model by Kanani et al. (2010).

5.1. Individual Rev Plots

5.1.1. Rev 271

Figure 4 shows an example plot from Rev 271, the first proximal Rev. As was noted by Bradley et al. (2020), an interval of magnetospheric quiet was observed prior to periapsis on Rev 271, when energetic particle fluxes were at near-minimum values. This Rev has therefore been categorized as a category 2 (green) Rev in this study (see Section 2 and Table 1). Figure 4a presents color-coded ion intensities from LEMMS channels A1-A4 spanning 35-606 keV for dominant protons as indicated on the right of the panel (see Roussos et al., 2018a, 2018b; Bradley et al., 2020, for more details). Figure 4b similarly shows color-coded electron intensities for LEMMS channels E0-E2 spanning 110–1350 keV as also indicated on the right. The typical time resolution of these data are ~5.2 s. Figure 4c and 4d present the B_ρ and B_z components of the residual magnetic field, in KGS cylindrical polar co-ordinates referenced to Saturn's spin/magnetic axis. These data are presented with 10 min resolution, to allow the large-scale field features to be clearly discerned. Figure 4e and 4f then show the cylindrical coordinates (ρ, z) of the spacecraft. Figure 4g presents the local time of Cassini.

As previously shown in Figure 2b, Cassini's apoapsis is displaced northward from the planetary equator, while the tail current sheet is displaced southward during these northern summer conditions. This results in Cassini

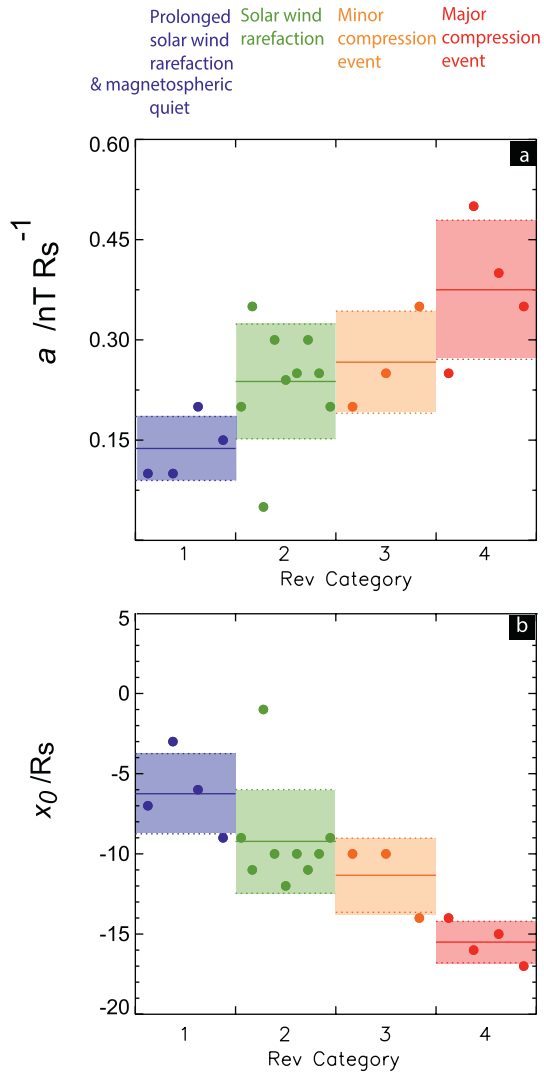

Figure 12. Box plots of the magnetopause and magnetotail fringing field parameters, a and x_0, in the same format as Figure 7.

mainly traversing the southern hemisphere plasma sheet as the spacecraft travels outbound after periapsis. This is confirmed by the LEMMS proton and electron fluxes in Figure 4a and 4b, which show significant increases above background levels as Cassini enters the plasma sheet after periapsis. As discussed by Bradley et al. (2020), LEMMS particle fluxes can be used to identify dynamical events, with the relative fluxes observed from Rev-to-Rev giving an indication of the magnetospheric state. Significantly enhanced plasma sheet particle fluxes are an indication of hot plasma injection and plasma sheet thickening in the inner tail. However, during this outbound trajectory through the plasma sheet no significant enhancement of energetic fluxes was detected in the plasma sheet compared to other "quiet" Revs. It is also evident that energetic fluxes and hot plasma were wholly absent during the inbound pass pre-periapsis, indicating that the spacecraft was located outside the main plasma sheet.

The measured residual B_ρ component of the field shown in Figure 4c (black line) presents a relatively gradual positive-to-negative gradient marking the dayside periapsis pass where Cassini crosses the magnetic equator. The residual B_ρ component switches sign with from negative-to-positive more abruptly but with significant fluctuations prior to apoapsis. The asymmetry in duration of negative B_ρ values relative to positive values simply reflects the spacecraft being predominantly located northward of the equatorial plane due to the orbital and seasonal effects as discussed above. The measured residual B_z component of the field shown in Figure 4d (black line), presents a steady increase from a few nT at a radial distance of ~18 R_s on the inbound pass, peaking at ~13 nT near the inner edge of the ring current at ~6 R_s. B_z then remains approximately constant as the spacecraft traverses inside the inner edge of the ring current, apart from small-scale perturbations near to periapsis on the dayside. On the outbound pass, B_z begins a steady decrease at a radial distance of ~7 R_s, again reaching a few nT at ~17 R_s where the spacecraft passes through the center of the current system where the residual radial field switches sign.

Overplotted in Figure 4 are four vertical black dotted lines marking $r = 4.25$ R_s and $r = 14$ R_s, both inbound and outbound. The data within these lines are plotted against a pink background. As described in Section 4.2, it is from within these lines that data were selected and fitted to our field model. In this region the black dotted line also shows the PPO-subtracted magnetic field data used in the fit (Section 4.2). As indicated above, the average amplitudes of the PPO oscillations are a few nT, so it is not always easy to differentiate by-eye the PPO-subtracted residual field from the residual field.

The best-fit parameters for the ring current model are presented at the top of Figure 4, determined as outlined in Section 4.3. The solid red lines overplotted in Figure 4c and 4d are the sum of the best-fit ring current and fringing field models, with the dashed red lines showing the fringing field only. There is close agreement between the model and the data both within the selected radial interval and outside this range. However, the model underestimates the magnitude of B_ρ at larger radial distances outbound. The solid blue lines in Figure 4c and 4d show the best-fit model from the analysis of Cao et al. (2020). For brevity, this model will be referred to as C2020. The C2020 model was determined using one CAN current disc, fitted to the magnitude of the magnetic field observed on the proximal orbits at a radial distance of between 1.5 and 3.8 R_s. This is inside the inner edge of the ring current (set at 6.5 R_s in our study), with the selected data covering about 19 h of local time, excluding only the midnight region. The C2020 study is then predominantly measuring the north-south ring current field near the center of the ring current. Figure 4c and 4d show that the C2020 model provides a good overall fit to the nightside ring current observations presented here, but underestimates the magnitude of the B_ρ component both inbound and outbound, and also models a B_z component which is

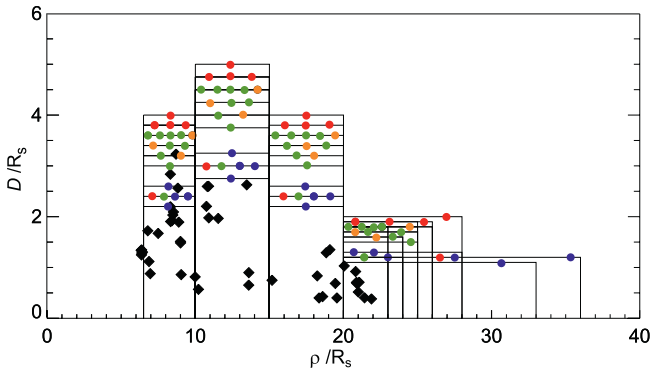

Figure 13. Presents the widths and half-thickness of the best-fit current discs for each of the proximal revs. Each Rev is color coded by its Rev category. The 47 black diamonds are the half-thickness measurements of Saturn's nightside ring current observed by Staniland et al. (2020).

more negative than that observed. We have calculated the RMS deviations (Equation 15) between the data and the nightside ring current model for both the C2020 model and our model. Selecting data in the radial range $4.25 < r < 14\ R_s$, the combined RMS deviation for the B_ρ and B_z components are 0.80 nT for our analysis, and 2.10 nT for C2020.

5.1.2. Rev 280

Figure 5 presents data for Rev 280 (category 4—red Rev) in the same format as in Figure 4. Bradley et al. (2020) described in detail the "major compression-response event" occurring during this Rev. A solar wind compression event is observed prior to periapsis, followed by PPO-modulated bursts of tail reconnection resulting in hot plasma injections, expansion of the plasma sheet, dipolarization of the field, and enhanced coupling currents. The effect of the bursts of tail reconnection are clearly observed in the LEMMS ion and electron data sets in Figure 5a and 5b, showing the spacecraft located within a region of enhanced energetic particle flux both on Cassini's inbound and outbound trajectory. Comparing the LEMMS ions and electrons from Rev 280 with those in Figure 4 for quiet Rev 271, it is clear that the nightside plasma regime is hotter and clearly expanded during Rev 280. Bradley et al. (2020) also reported that, in effect, the characteristic hinging distance of the current sheet is reduced on Rev 280 due to the effect of the enhanced solar wind dynamic pressure on the tail field orientation. Our modeled field (solid red line in Figure 5c and 5d) again provides close agreement with the observed ring current signatures, while the C2020 model (solid blue line) under-estimates the magnitude of the nightside B_ρ component both inbound and outbound. Our modeled B_z component agrees well with the overall shape of the observed ring current signature for both the inbound and outbound portions of the trajectory, while the C2020 model underestimates the nightside B_z component observed both inbound and outbound. The RMS deviations of the field models determined for Rev 280 are the largest determined for the proximal Revs, indicative of the ongoing disturbed magnetospheric conditions on this Rev. The RMS deviation is 2.13 nT for our model and 7.04 nT for the C2020 model.

5.1.3. Rev 288

In Figure 6, we show data from Rev 288 in the same format as Figures 4 and 5. Similar to Rev 280, Bradley et al. (2020) identified a major compression-response event occurring during this Rev (event K* in their study), so it has been categorized as a category 4-red Rev. This compression event was unanticipated from the ongoing heliospheric modulations at the solar rotation period, and was associated with a solar energetic proton event, indicating the approach and impact of an interplanetary shock. The effects of this event are observed in magnetic field, particle and SKR signatures. The LEMMS ion and electron data in Figure 6a and 6b show a clearly enhanced and expanded plasma sheet compared to Revs 271 and 280. The C2020 model provides an excellent fit to B_z on the inbound trajectory and throughout the ring current region. However, C2020 underestimates the magnitude of the nightside B_z component at larger radial distances outbound, and also underestimates the nightside B_ρ component, particularly in the inbound region. The RMS deviation between the data and the model is 1.49 nT for this model, compared to 5.51 nT for the C2020.

5.2. Summary of LEMMS Protons and Electrons Observations

Bradley et al. (2020) used magnetic field data, low-frequency extensions of the SKR, and LEMMS energetic particle data to determine Saturn's magnetospheric response to solar wind conditions during the proximal Revs. The individual Rev plots presented in Section 5.1 demonstrate how Saturn's plasma sheet is enhanced and expanded during Revs 281 and 288 that are major compression-response Revs (category 4-red), compared with the quiet magnetospheric conditions during Rev 271 (category 2-green). To study the plasma sheet electrons and ions in more detail, we have calculated the mean value of the LEMMS electron intensity for energy channel E0 and the LEMMS proton intensity for the ion energy channel A1. The mean values are determined for observations made between $r = 4.25$ and $14\ R_s$ when Cassini traverses the plasma sheet on its outbound trajectory.

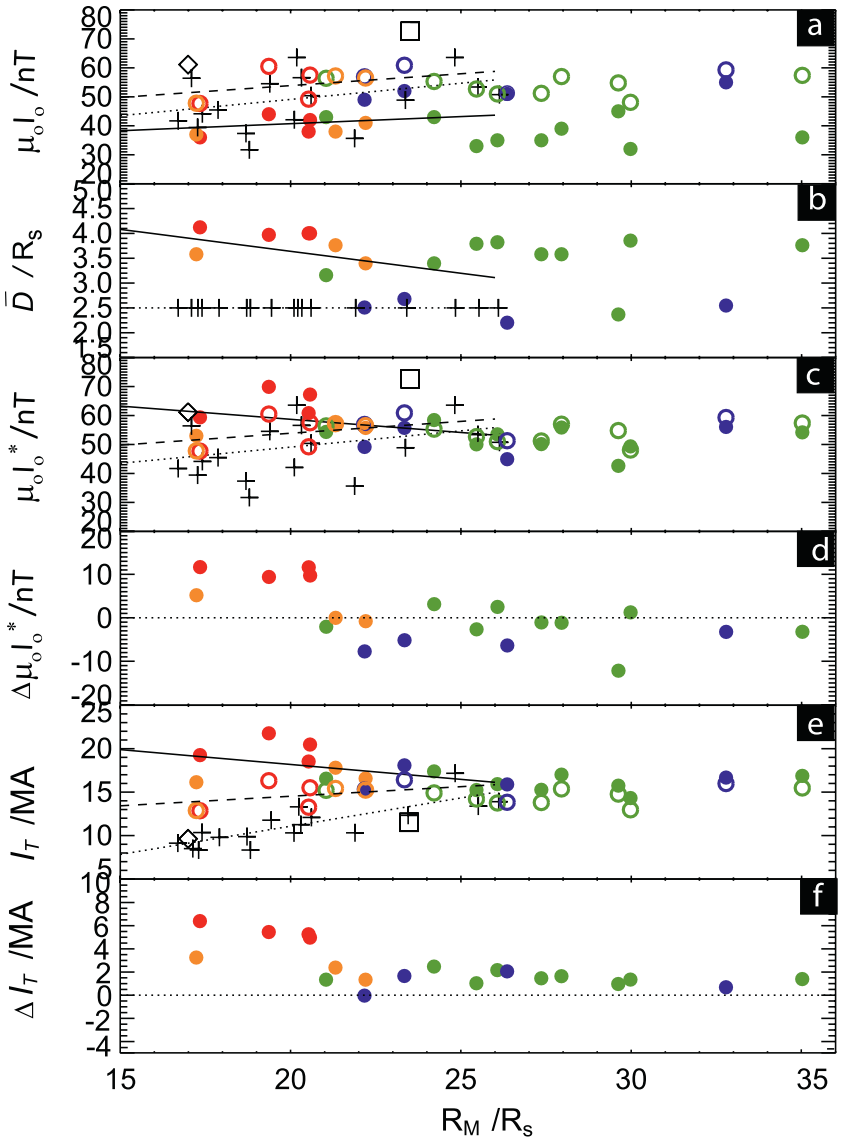

Figures 14. (a), (b), (c), (d) and (e) Plots the ring current parameters $\mu_0 I_0$, $\bar{D}$, $\mu_0 I_0^*$, and I_T, respectively. The filled colored circles present the data determined in this study, the open circles show the results from C2020. Both results are color-coded according to Rev category and plotted versus subsolar magnetopause distance, R_M, as determined using the model of Kanani et al. (2010). The results determined by B2007 are shown as black crosses. B2007 also included data from the Pioneer-11 (diamond) and Voyager-1 (square) flybys. Dotted black lines are linear least square fits determined by B2007, valid to an outer limiting R_M value of ~26 R_S. Linear fits to the data presented in this study are shown by the solid black lines, and linear fits to C2020 are shown as dashed black lines. (d) presents $\Delta\mu_0 I_0^*$, the difference between $\mu_0 I_0^*$ determined in this study and the $\mu_0 I_0^*$ determined by C2020. (f) presents ΔI_T, the difference between I_T determined in this study and the I_T reported by C2020.

The results are presented in Figure 7 as two box plots. Figure 7a shows the mean intensity of ion energy channel A1 (35–56 keV), and Figure 7b shows the mean intensity of the electron energy channel E0 (110–365 keV). The colored circles give the values from the individual Revs, color-coded by Rev category. For each of the Rev categories the solid lines give the mean intensity values and the shaded regions bound by two dashed lines give their standard deviation. Again, these "boxes" are color-coded according to the Rev category. Rev 276 is excluded from the red category describing major compression-response events, because the solar wind and magnetospheric conditions varied while Cassini traversed the ring current region, resulting in a ring current which is markedly different to the other red Revs.

The results show that during the blue Revs, associated with prolonged magnetospheric quiet, the lowest proton (~40 ± 10 /cm^2 sr s keV) and electron (~6 ± 5 /cm^2 sr s keV) intensities are observed, while significantly enhanced proton (~860 ± 190 /cm^2 sr s keV) and electron (50 ± 40 /cm^2 sr s keV) intensities are observed during the red major compression-response Revs. These observations are consistent with PPO-modulated bursts of tail reconnection resulting in hot plasma injections and expansion of the plasma sheet. These results, although not unexpected, give an interesting indication into the life cycle of dynamical configurations and injections in Saturn's ring current. Often, red and blue Revs occur consecutively i.e. they are separated in time by less than a week (see Figure 8). The significant differences in particle intensity between the red and blue Revs demonstrate that the enhanced particle injection and expanded plasma sheet observed during a tail reconfiguration event lasts for less than seven days. Bradley et al. (2020) reported that the high LEMMS flux regimes produced by compressions prevail between inbound and outbound passes, so over a day or two, but these enhanced particle fluxes don't endure from a compressed orbit to a following quiet one (approximately one week later). In essence, Saturn's ring current plasma is frequently recycled and reconfigured.

5.3. Summary of Ring Current Parameters

Figures 8a–8i present a summary of the best-fit ring current and fringing field parameters determined on a Rev-by-Rev basis for all full proximal Revs, 271–292 (except Rev 277 which was excluded due to significant data gaps within the main ring current region). For each Rev, the parameters are plotted at the time of periapsis, which is also labelled at the top of the figure. The results in Figure 8 are also tabulated in Table 2, color coded in the same manner. In addition to the six model ring current and fringing field parameters, described in Section 3.2, we also derive three additional parameters, the total ring current I_T, k_{RC} the ratio of the magnetic moment of the ring current to the magnetic moment of the planetary dipole, and $\bar{D}$ the mean half thickness of the ring current D (Equations 12-14). Table 2 also presents the RMS deviation between the best-fit model and the data for each Rev (Equation 15). In addition to the model parameters shown in Figures 8a–8i, in Figures 8j we show the PPO beat phase (Equation 2). During the proximal Revs, the PPO beat cycle period is ~42.5 days, so that the interval studied corresponds to ~3.25 beat cycles. Expected tail thinning conditions are highlighted on the plot by the vertical grey bars showing intervals during which the beat phase lay in the range $90^o < \Delta\Phi < 270^o$, centered on antiphase.

Figure 8k also shows the solar wind dynamic pressure propagated to Saturn using an MHD code initialized using OMNI (Operating Missions as a Node on the Internet) data obtained near ~1 AU (Tao et al., 2005, also discussed in Bradley et al., 2020). As discussed in more detail by Bradley et al. (2020), under the conditions prevailing during this interval the likely uncertainties in the timing of arrival of dynamic pressure fronts is likely to be less than ±35 h (Zieger & Hansen, 2008). The proximal Revs studied here span ~130 days, thus corresponding to ~5 solar rotation periods of solar wind disturbances. The vertical dashed lines in Figure 8, spaced at 26 day intervals, mark the approximate times of cyclical minima in the galactic cosmic ray flux observed in LEMMS data, and the approximate times of minima in the propagated solar wind dynamic pressure which result from heliospheric modulations at the solar rotation period (Bradley et al., 2020). It can be seen that with the exception of the first full such interval in Figure 8k when two compressions occurred, one CIR-related compression was observed during each solar rotation period, leading to sharp increases in dynamic pressure typically by more than an order of magnitude. In addition a non-recurrent ICME event occurred during Rev 288 as discussed above.

An initial inspection of Figure 8 suggests that many of the ring current and fringing field parameters undergo semi-cyclical variations, showing four or so peaks during the ~130 days interval studied here. As the beat period (~42.5 days) and the solar rotation period (~26 days) are somewhat similar during these proximal Revs, further analysis is needed to determine whether the ring current parameters are modulated by the PPO beat phase, the variable solar wind dynamic pressure, or both. Overall, therefore, these proximal Revs allow the study of the ring current response to a significant number of solar wind compression events over a range of PPO conditions, thus allowing examination of the influences of both.

5.4. Variation of Ring Current Parameters with Solar Wind and Magnetospheric Conditions

In order to study the response of the ring current to varying solar wind and magnetospheric conditions, we have calculated the mean and standard deviation (SD) of each ring current parameter for the four Rev categories. The results for $\mu_0 I_0$, k_D, R_2, and R_H are presented as four box plots in Figure 9, shown in the same format as Figure 7.

The colored circles give the values from the individual Revs (as also presented in Figure 8 and Table 2), again color-coded by Rev category. The mean and SD of all the parameters are presented in Table 3.

Figure 9a shows the box plot for the current density parameter, $\mu_0 I_0$. During intervals of moderate solar wind rarefaction (green Revs) and during intervals of solar wind compression (orange and red Revs), the mean current density of the ring current are equal within uncertainties ($\mu_0 I_0 = 37.9 \pm 4.8$, 38.7 ± 2.1 and 40.0 ± 3.7 nT, for the green, orange, and red Revs, respectively). During intervals characterized by prolonged solar wind rarefaction (blue Revs), however, $\mu_0 I_0$ is significantly enhanced compared with all the other intervals ($\mu_0 I_0 = 51.8 \pm 2.5$ nT). The overall magnitude of the field observed by the spacecraft will mainly depend upon the total current flowing in the disc, which for an essentially fixed radial structure, is dependent not only on the current parameter but also on its thickness. Figure 9b presents k_D, the thickness scaling constant and Figure 10a presents the related $\bar{D}$, the mean half-thickness of the ring current (Equation 13). For the blue Revs, the ring current is significantly thinner ($k_D = 1.20 \pm 0.08$ and $\bar{D} = 2.48 \pm 0.20\ R_s$) than during the other intervals (the mean values for the three other intervals being $k_D = 1.73 \pm 0.19$ and $\bar{D} = 3.63 \pm 0.43\ R_s$). Within uncertainties k_D and $\bar{D}$ are equal for the orange and green Revs, demonstrating that the thickness of the current sheet is similar during rarefied/moderate and compressed solar wind conditions, as long as the PPOs are in phase during the solar wind compressions so that tail reconnection is not favored to occur. However, k_D and $\bar{D}$ are significantly enhanced during major compression-response events ($k_D = 1.93 \pm 0.05$ and $\bar{D} = 4.02 \pm 0.07\ R_s$ for the red Revs). These results indicate that the ring current is modulated by the magnetospheric response to external solar wind conditions, and that this response is determined by the relative phasing of the PPOs, with the injection of hot plasma during tail reconnection events enhancing the thickness of the ring current. Comparing Figure 9a with Figures 9b and 10a demonstrates that during times of prolonged solar wind rarefaction there is an anti-correlation between the density and the thickness of the current sheet, with the thinnest ring current being associated with the largest current density.

Figure 9c presents the outer radius of the ring current, R_2. Within errors R_2 is comparable for all the Rev categories, with the mean values varying between $R_2 = 25.0 \pm 1.0\ R_s$ for the orange Revs and $R_2 = 27.8 \pm 3.9\ R_s$ for the blue Revs. However, studying the R_2 values from the individual Revs shows that the outer radius of the ring current varies by ~50% during these proximal Revs, ranging from a minimum radial extent of 23 R_s to a maximum of 36 R_s. The summary plot (Figure 8) shows that the two Revs with the most extended ring current (Revs 278 and 282) occur during intervals of solar wind rarefaction and are associated with the thinnest ring current, demonstrating that during these intervals the nightside ring current becomes thin and elongated.

Figure 9d presents the hinging distance, R_H. We have considered the maximum hinging distance that we can accurately determine in this study. We have fitted the ring current model to magnetic field data observed within a radial distance of 14 R_s. Using Equation 7, we calculate that during northern summer conditions a current sheet hinged at 35 R_s will be displaced south of the equatorial plane by 0.5 R_s at a radial distance of 14 R_s, while a current sheet hinged at 40 R_s will be displaced 0.3 R_s south of the equatorial plane at this radial distance. We estimate that within the scatter of the data it may not be possible to accurately detect displacements of the current sheet below 0.5 R_s, so the maximum possible hinging distance that can be detected in this study is set to 35 R_s. Figure 9d shows that, within errors, the mean R_H is equal within all four categories. However, during the 13 Revs which occur during solar wind rarefactions (blue and green Revs), only three have hinging distances of less 35 R_s. This compares with four out of the seven Revs occurring during solar wind compressions (orange and red Revs). This suggests that the current sheet hinging distance for intervals of solar wind rarefaction, occurring during northern hemisphere summer, may be too large to be accurately determined in this study. Furthermore, the mean values are smaller and the error bars much wider during intervals of solar wind compression than during solar wind rarefactions, with the smallest hinging distances being observed during intervals of solar wind compression. These results would suggest, as expected, that the hinging distance of the current sheet is reduced when the magnetosphere is compressed by the solar wind.

Figure 10 presents box plots of the three parameters derived from the fitted ring current parameters; Figure 10a shows the mean ring current thickness $\bar{D}$ (Equation 13), Figure 10b shows the total current I_T (Equation 12), and Figure 10c presents k_{RC}, the ratio of the ring current magnetic moment relative to the magnetic moment of Saturn's dipole field (Equation 14). The ring current is significantly thinner during intervals of magnetospheric quiet associated with prolonged solar wind rarefactions ($\bar{D} = 2.4 \pm 0.2\ R_s$, for the blue Revs) than during magnetospheric storms ($\bar{D} = 4.0 \pm 0.1\ R_s$ for the red Revs). However, here we can see that for the blue Revs the high

current density parameter and narrow current sheet combine to produce a ring current carrying a total current which is similar to the total current carried during intervals of solar wind rarefaction (green Revs) and during minor compression-response events (orange Revs). $I_T = 16.5 \pm 1.2$, 16.0 ± 1.0, and 16.8 ± 0.9 MA, for the blue, green, and orange Revs, respectively. Modeling work by Persoon et al. (2009) suggests that the width of the plasma sheet is essentially proportional to the square root of the ion parallel temperature and inversely proportional to the square root of the ion mass. Such a thin ring current suggests a current sheet dominated by cold Enceladus water group ions (Persoon et al., 2009, 2020). During major compression-response events I_T is significantly increased compared to all other events ($I_T = 20.0 \pm 1.4$ MA for the red Revs). Tail reconnection during these major compression-response events increases the thickness of the ring current and the total current it carries.

Figure 10c presents k_{rc}, the ratio of the ring current magnetic moment relative to the magnetic moment of Saturn's dipole field. k_{rc} is equal during all intervals except during major compression-response events. So, $k_{rc} = 1.11 \pm 0.24$, 0.97 ± 0.25, and 0.96 ± 0.10 for the blue, green and orange Revs, respectively, while k_{rc} is increased to 1.21 ± 0.13 for the red Revs. Considering that both the red and orange Revs occur during intervals of solar wind compressions but at different times of the PPO beat cycle. The increase in k_{rc} for the red major compression-response events occurring during PPO antiphase conditions, clearly demonstrates that it is the magnetospheric response to the solar wind conditions, conditioned by the relative phases of the PPOs, that results in modulations of the ring current and enhances its magnetic moment.

In Figure 11, we present box plots of two parameters which can "drive" Saturn's magnetosphere. Figure 11a presents the mean and standard deviation of the PPO beat-phase (shown in Figure 8j) for the four Rev categories, as well as for the individual Revs. For each Rev the mean beat phase has been determined over the time interval selected for fitting the ring current model, using directional statistics (Mardia & Jupp, 2000). As previously reported by Bradley et al. (2020), there is a statistically significant difference in the mean PPO beat phase between major and minor compression-response events, with major compression-response events occurring close to PPO antiphase conditions and minor compression-response events close to PPO in phase conditions ($\Delta\Phi = 200 \pm 53°$ and $\Delta\Phi = 335 \pm 29°$ for red and orange Revs, respectively). Figure 11b similarly presents a box plot of the propagated solar wind density, with the mean density calculated on a Rev-by-Rev basis over a time interval spanning 1.5 days either side of periapsis. As expected, the Revs associated with solar wind compressions have a larger mean solar wind dynamic pressure than the Revs occurring during solar wind rarefactions. We further note that the four magnetospheric quiet Revs are associated with extended intervals of solar wind rarefaction and PPO antiphase conditions ($\Delta\Phi = 151 \pm 84°$ for the blue Revs). This suggests that BOTH solar wind compressions and PPO antiphase conditions are needed for major magnetospheric disturbances, resulting in significant modulations of the ring current, to occur at Saturn.

B2007 analyzed how Saturn's ring current was modulated by the system size of Saturn's magnetosphere, parameterized by the position of the subsolar magnetopause, as we will describe in Section 6. During the proximal orbits, of course, the spacecraft remained distant from the magnetopause throughout. We therefore estimate the subsolar magnetopause position using the model of Kanani et al. (2010).

$$R_M = a_1 P_{dyn}^{-a2} \tag{16}$$

where $a_1 = 10.3\ R_s$ /nPa and $a_2 = 0.2$, and P_{DYN} is the mean solar wind dynamic pressure (in nPa) presented in Figure 11b. Figure 11c then shows a box plot of the mean magnetopause stand-off distance for the four Rev categories, with the values from the individual Revs shown by colored circles, as before. As expected, the magnetopause stand-off distance is significantly decreased during major compression-response events compared to intervals of solar wind rarefaction.

5.5. Variations of the Magnetotail and Magnetopause Fringing Fields

In this study, we have included a simple model for the divergence-free and curl-free (i.e. no local current) magnetotail and magnetopause fringing fields (Equations 10 And 11). The modeled fringing fields are shown in the Rev plots in Figures 4–6 as red dashed lines, and contribute approximately 10% to the total field in the ring current region. The fringing field parameters are a and x_0, where a is gradient of the fringing fields for both the B_x and B_z components, and x_0 is the position on the planetary equator where the positive B_z field of the inner magnetotail field gives way to the negative B_z of the magnetopause field extending

into the dayside. Figure 12a and 12b present box plots of a and x_0, respectively. Both parameters are clearly organized by the Rev category, with the gradient a increasing and x_0 becoming increasingly negative as the solar wind dynamic pressure and magnetospheric disturbance levels are enhanced. The increased negative x_0 means that, as the solar wind compressions of the magnetosphere increase, this zero-point for the B_z component of the fringing fields moves from near the planet into the tail.

6. Comparison with Previous Studies

6.1. Comparison with Staniland et al. (2020) and Carbary (2019)

Staniland et al. (2020) analyzed magnetic field data from 66 Cassini Revs, selecting orbits when the spacecraft made fast and steep crossings of the equatorial current sheet which allowed for direct determination of the current sheet thickness. Current sheet crossings were identified directly from the magnetic field data by reversals in the B_ρ component of the field, as well as additional criteria. 47 thickness measurements were made of the nightside ring current, covering three hours of local time either side of local midnight, in the radial range from ~5.5 to 22 R_s. These nightside observations spanned most of the duration of the Cassini mission, stretching from Rev 37 (starting January 2007) to Rev 239 (ending August 2016). However, no measurements were included from the 2017 proximal orbits studied here, as Cassini was not moving fast enough north to south to determine the current sheet thickness directly. Staniland et al. (2020) calculated the mean thickness values both inside the region described as the quasi-dipolar magnetosphere ($r < 15\ R_s$), and beyond this region defined as "magnetodisc proper" (Arridge et al., 2008). On the dayside, the average half-thickness was found to be 1.1 R_s within the quasi-dipolar region, and 1.4 R_s within the magnetodisc proper. On the nightside the current sheet half-thickness was 1.7 R_s within the quasi-dipolar region, decreasing to 0.7 R_s within the magnetodisc proper region. The nightside ring current can therefore be described as teardrop shaped, becoming significantly thinner with increased radial distance.

In Figure 13, we present a comparison of our results with the results of Staniland et al. (2020), where we plot the half-thickness of the four current discs as a function of radial distance for each of the proximal Revs color-coded by its Rev category. As previously discussed, the thickest ring current is associated with major compression-response events, while the thinnest ring current is observed during prolonged solar wind rarefaction intervals. The 47 black diamonds over-plotted on the figure are the half-thickness measurements of Saturn's nightside ring current observed by Staniland et al. (2020). Clearly, we determine a significantly thicker ring current, with the mean value of the proximal ring current half-thicknesses approximately twice as large as that determined by Staniland et al. (2020) ($<\overline{D}> = 3.36 \pm 0.62\ R_s$ and $1.38 \pm 0.76\ R_s$, respectively). We have considered whether our initial assumption, of a ring current with a half-thickness of $D = 2.5\ R_s$, might predetermine the thicker modelled ring current reported here. We therefore repeated the analysis, defining $D = 1.25\ R_s$ in Step 1. This resulted in a modelled ring current with a mean value of $<\overline{D}> = 3.21 \pm 0.62\ R_s$. This is identical within errors to our mean thickness reported in Figure 13, meaning that the discrepancy between the thickness of the ring current found in this study compared to that reported by Staniland et al. (2020), cannot be explained by the initial assumptions made in our ring current modelling.

To investigate this discrepancy in thickness further we return to Figure 2b, showing the thickness of the ring current in the midnight sector modeled by Carbary (2019). Our initial ring current model, comprising four CAN discs with initial thickness of 2, 2.5, 2 and 1 R_s centered on the Arridge et al. (2008) warped magnetodisc equator, is overplotted in Figure 2b as shaded white blocks. Overplotted in Figure 2b are also the ring current thicknesses for each Rev. These half-thickness measurements are presented in Figure 13, but now we show the full thickness of the ring current by symmetrically extending our modeled values to either side of the current sheet center. Our results are shown as white lines and colored circles with white edges. The 47 thickness measurements from Staniland et al. (2020), presented in Figure 13 as black diamonds, are shown in Figure 2b as black lines, also symmetrically extended to either side of the center of the current sheet. Studying Figure 2b we can see that both sets of results show some features of similarity in the decrease of ring current thickness with radial distance. However, the ring current thicknesses from Staniland et al. (2020) roughly follow the outer boundary of Carbary's more intense ring current contours shown in green and light blue, where the current density reaches ~0.1–0.15 MA/R_s^2. The outer model boundary of our modeled current sheet thickness, corresponding to the maximum thickness constant $k_D = 2$ determined for Rev 280, approximately follows the ~0.05 MA/R_s^2 contour of Carbary (2019).

In this study, we modeled the ring current signature observed over a wide radial distance range $4.25 < r < 14\ R_s$, while Staniland et al. (2020) determined the current sheet crossings from abrupt deflections in the magnetic field. These deflections may correspond to the width of the most intense current carrying region, and may not capture the weaker current carrying region outside this which still leaves a detectable signature in the magnetic field. Finally, the outer edges of the modeled ring current of Carbary (2019) are thicker than the proximal ring current modeled here. However, Carbary's results suggest that the current intensity peaks near the center of the sheet and decreases with increasing z. The CAN current model requires the current intensity to be constant with z, an assumption that will result in a reduced modeled ring current thickness compared to the ring current determined by Carbary (2019) for the same total current.

6.2. Comparison with Dawn and Dayside Ring Current Modeling by Bunce et al. (2007) and Proximal Ring Current Modeling of Cao et al. (2020).

B2007 studied Saturn's ring current from magnetic field observations recorded in Saturn's dawn and dayside magnetosphere during the first two years of the Cassini mission. During this interval the ring current region was traversed near the equatorial plane in the morning and near-noon sector on the inbound pass, and in the post-midnight and dawn sector on the outbound pass. B2007 examined the residual magnetic field observations, and fitted a single CAN ring current model to the ring current in the middle magnetosphere. They could not determine the thickness of the current sheet directly and so employed a fixed current sheet half-thickness of 2.5 R_s for all the Revs, based on the Voyager and Pioneer results. B2007 examined the variation of the ring current parameters with system size, where the system size was given by the subsolar magnetopause distance, R_M, determined from the magnetopause positions observed on the inbound passes of these orbits mapped to the subsolar point.

C2020 also modelled the ring current on Cassini's proximal Revs. They selected data between 1.5 and 3.8 R_s, well inside the inner edge of the ring current. This data covered about 19 hours of local time, corresponding to all local times except for the midnight region. The C2020 study then predominantly measured the north-south ring current field near the center of ring current. The C2020 model used fixed radii for the inner and outer edges of the current sheet,6.5 and 20 R_s respectively, and a fixed current sheet half-thickness $D = 2.5\ R_s$. They determined $\mu_0 I_0$ for each of the proximal Revs.

In Figure 14, we show the ring current parameters plotted versus subsolar magnetopause distance, R_M, with our results shown as closed circles and the results from C2020 shown as open circles, both color coded in the usual manner. As presented in Figure 11c, we estimate the position of the subsolar magnetopause during the proximal orbits using the modeled dynamic pressure and the Kanani et al. (2010) formula. Figure 14 shows that the orange and red Revs, indicating disturbed conditions during solar wind compressions, are generally associated with magnetopause stand-off distances $R_M \lesssim 22\ R_s$, while the blue and green Revs, indicative of quiet magnetospheric conditions during solar wind rarefactions, have larger values of magnetopause stand-off distances $R_M \gtrsim 22\ R_s$. This gives confidence that averaging the propagated solar wind dynamic pressure, over a three day interval centered on periapsis, gives a good indication of the solar wind conditions and therefore of the magnetopause stand-off distances. The results determined by B2007 are shown as black crosses. B2007 also included data from the Pioneer-11 (diamond) and Voyager-1 (square) flybys. Overlaid on the plots as dotted black lines are linear least square fits determined by B2007, valid to an outer limiting R_M value of ~26 R_s, representing the maximum R_M value determined in that study. Although a few of our proximal data points are estimated to correspond to larger R_M values, here we have similarly limited linear fits to data within $R_M \leq 26\ R_s$, shown by the solid black lines for our results and by the dashed line for the C2020 results, in order to make direct comparisons.

Figure 14a presents the current density parameter $\mu_0 I_0$ plotted versus R_M. Both on the dayside and the nightside $\mu_0 I_0$ increases with increasing magnetopause stand-off distance, at least within $R_M \leq 26\ R_s$. In Section 5.4, we showed that significantly enhanced current density values are observed during the quiet Revs associated with prolonged intervals of reduced solar wind dynamic pressure, that is, when Saturn's magnetosphere is enlarged and its magnetopause stand-off distance extended. The best-fit line for the B2007 dawn/dayside

data has a gradient that is approximately twice as large as the best-fit line to the proximal nightside dataset determined in this study (1.12 nT R_s^{-1} for the B2007 data and 0.52 nT R_s^{-1} for the proximal nightside data), with the linear fit to the dayside data remaining larger than the fit to the nightside data within $15 \leq R_M \leq 26\ R_s$.

In Figure 14b, we plot a measure of the current sheet half-thickness, $\bar{D}$, (Equation 13). Both B2007 and C2020 used a fixed current sheet thickness for all the Revs. The half-thickness of the nightside current sheet is predominantly larger than 2.5 R_s, but decreases with increasing magnetopause stand-off distance, with the thickest ring current observed during solar wind compressions when R_M is decreased. To a first approximation, for a current disc of given radial extent, the field generated is proportional to the total current carried, which is related to the product of the current density parameter and the thickness. In Figure 14c, we therefore show the current density parameter, $\mu_0 I_0$*, that would produce a similar field to that observed given an assumed half-thickness of 2.5 R_s as in B2007 and C2020, given by

$$\mu_0 I_0 * = \mu_0 I_0 \times \left(\bar{D} / 2.5\right) \tag{17}$$

$\mu_0 I_0$* show a general decreasing trend with increasing system size on the nightside, but an increasing trend with increasing system size on the dayside. We can see that during intervals of solar wind rarefaction, associated with large magnetopause stand-off distances, similar values of $\mu_0 I_0$* are observed on the dayside and the nightside. During solar wind compressions, however, larger values of $\mu_0 I_0$*are observed in the midnight region than at other local times. For a compressed magnetosphere, the values reported by B2007 are slightly smaller than the values reported by C2020.

Figure 14d presents $\Delta\mu_0 I_0$*, the difference between the nightside $\mu_0 I_0$* determined in this study and the $\mu_0 I_0$* reported by C2020 for the proximal Revs. The values are approximately the same during intervals of solar wind rarefactions. However, during solar wind compressions when $R_M \leq 21\ R_s$, $\mu_0 I_0$* is approximately ~10 nT larger in the midnight sector than at other local times.

In Figure 14e, we present the total ring current, I_T, calculated using Equation 12. When the subsolar magnetopause is expanded beyond ~25 R_s, the total current is approximately ~15 MA on both the dayside and the nightside. However, when the magnetosphere is compressed and R_M ~17.5 R_s, the current on the nightside increases to ~20 MA, but decreases in the dayside/dawn sector to ~10 MA (B2007) and to ~14 MA (C2020), associated with a less developed magnetodisc field under these conditions. This is shown in Figure 14f which presents ΔI_T, the difference between the nightside I_T reported here and the I_T reported by C2020. The values of I_T are approximately the same during quiet solar wind conditions, but I_T is ~6 MA larger on the nightside compared to the dayside during compressed intervals when $R_M < 21$–$22\ R_s$.

These findings are consistent with a picture in which, under solar wind rarefaction conditions of magnetospheric quiet, the disc currents close essentially wholly around the planet. However, during major compression-response events, a significant fraction of the nightside current, essentially equal to the difference between the two data sets as presented in Figure 14f does not close via the dayside ring current/magnetodisc region. Instead, the current in the outer nightside region must form a significant partial ring current, closing either via the magnetopause or the planetary ionosphere. These currents are no doubt carried principally by the hot plasma injected into the nightside region during tail reconnection occurring during major compression-response events, as discussed above. Since this partial nightside ring current is observed to persist over several planetary rotations, we suggest that during intervals of solar wind compression the outer part of the nightside current sheet is more akin to an enhanced tail current system than a ring current which closes round the planet.

7. Summary and Conclusion

In this study, we have examined the nightside ring current as observed on 21 proximal periapsis passes during Saturn's Grand Finale. We fit a modified CAN current disc model, teardrop-shaped with four CAN discs of variable half-thickness and outer radial extent, to the observed magnetic field on each of these Revs, to determine the current density parameter $\mu_0 I_0$, the thickness scaling ratio k_D and the outer edge of the ring current, R_2. Our model also takes account of the magnetotail and magnetopause fringing fields,

and the tilt of the current layer by solar wind forcing. We then refer to the work of Bradley et al. (2020) who categorized each proximal Rev by the prevailing solar wind and magnetospheric conditions, from very quiet conditions occurring during solar wind rarefactions to major compression-response events occurring when the PPOs were in antiphase. Based on this work, we categorize the proximal Revs into four categories, and then examine the behavior of the nightside ring current for different solar wind and magnetospheric conditions. We compare our results with previous studies, examining the dayside ring current (Bunce et al., 2007), an initial study of Saturn's ring current during the proximal passes (Cao et al., 2020) and the ring current during the Cassini mission (Staniland et al., 2020). Our main results are as follows:

1) Saturn's ring current is influenced by both external and internal drivers, as is Saturn's magnetosphere as a whole. The external driver is the solar wind while the internal driver is the PPO phenomenon
2) On the nightside, the current density of the ring current is similar during intervals of solar wind compression and intervals of moderate solar wind rarefaction ($\mu_0 I_0 = 37.8 \pm 4.8$, 38.7 ± 2.1, and 40.0 ± 3.7 nT for the green, orange, and red Revs, respectively). However, during intervals of magnetospheric quiet associated with prolonged solar rarefactions, the current density is enhanced by approximately a third ($\mu_0 I_0 = 51.8 \pm 2.5$ nT for blue Revs).
3) The half-thickness of the nightside ring current is similar during intervals of moderate solar wind rarefaction and during minor compression-response events, with $\bar{D} \sim 3.5\ R_s$. However, during major compression-response event, the half-thickness is enhanced by ~15% to $\bar{D} \sim 4\ R_s$, while during intervals of magnetospheric quiet occurring during prolonged solar wind rarefactions the ring current half-thickness is reduced by ~30% to $\bar{D}$ ~2.5 R_s
4) The total current carried by the nightside ring current is similar during all intervals, except when major compression-response events are observed. Apart from these times, the mean total current $I_T = 16.3 \pm 1.0$ MA. During magnetospheric compression events, an increase in the thickness of the ring current results in an increase in the total ring current by ~20% to $I_T = 20.0 \pm 1.4$ MA, consistent with a ring current populated by hot plasma injected from the nightside by tail reconnection events.
5) During intervals of prolonged solar wind rarefactions, the total current carried by the nightside ring current does not increase compared to other non-major compression-response intervals, despite the significantly enhanced ring current densities at these times. This is because the ring current is also much thinner during these very quiet Revs ($I_T = 16.5 \pm 1.2$, 16.0 ± 1.0, 16.8 ± 0.9 MA, and $\bar{D} = 2.48 \pm 0.2$, 3.47 ± 0.47, 3.57 ± 0.18 R*s* the blue, green and orange Revs, respectively). These results are consistent with an increased influence of cool, dense, water group ions from Enceladus, centrifugally confined to Saturn's equatorial plane, during these very quiet Revs.
6) During intervals of solar wind rarefactions, associated with enhancements in the size of Saturn's magnetosphere, the dayside/dawn and nightside ring currents have similar current densities and total current ($\mu_0 I_0$~52 nT, I_T~15 MA). This is consistent with the formation of a magnetodisc in which the current closes essentially wholly around the planet within the radial range to ~25 R*s*
7) When Saturn's magnetosphere is compressed the total current decreases by about by ~10 MA in the dayside/dawn sector, indicative of a less developed magnetodisc field configuration (Bunce et al., 2007). During major compression-response events, occurring during PPO antiphase conditions, the total current on the nightside increases by about a third from $I_T \sim 15$ MA to $I_T \sim 20$ MA. This indicates the existence of a partial nightside ring current under these circumstances, populated by hot plasma injected from the nightside when tail reconnection occurs. This increase in the hot plasma content of the ring current is clearly observed in the LEMMS proton and electron data during major compression-response events. This partial ring current must close partly via magnetopause currents and possibly partly via field-aligned currents into the ionosphere.
8) The nightside ring current modeled here is thicker than the nightside ring current measured by Staniland et al (2020) from the spatial gradients in the magnetic field data. Carbary (2019) determined averaged empirical models of the thickness of the ring current from Cassini's magnetic field data. We find that the Staniland et al. (2020) ring current agrees with the more intense ring current region determined by Carbary (2019). The maximum thickness of the ring current detected here on the proximal Revs is slightly smaller than the outer boundary region presented by Carbary (2019). It may be that the main current sheet crossing signatures detected by Staniland et al. (2020) represent the boundary of the most intense ring current, but there is a gradual decline in ring current intensity beyond this which also has an associated magnetic field signature.

9) The magnetotail and magnetopause fringing fields are clearly modulated by solar and magnetospheric conditions, with the gradient a increasing and x_0, the zero-point for the B_z component of the fringing fields, moving from near the planet during quiet times and into the tail as solar wind compressions and magnetospheric disturbance increases.

Appendix 1: Definition of Parameters

$\bar{D}$ —the mean half-width of the ring current

D_n—the half thickness of ring current disc n

I_T —the total current in the ring current

k_{RC}—the ratio of the magnetic moment of the ring current to the magnetic moment of the planetary dipole

$R_{1,n}$—the inner cylindrical radii of disc n

$R_{2,n}$—the outer cylindrical radii of disc n

R_H—the hinging distance of the current sheet

Z_{cs}—distance from the planetary equatorial plane to the current sheet

Φ_N—global phase of the northern PPO system

Φ_S—global phase of the southern PPO system

$\Delta\Phi$—PPO beat phase

θ_{SUN}—the direction of the solar wind flow (defined as the negative of the subsolar latitude)

Data Availability Statement

Calibrated magnetic field data from the Cassini mission are available from the NASA Planetary Data System at the Jet Propulsion Laboratory (https://pds.jpl.nasa.gov/).

Acknowledgments
Work at the University of Leicester was supported by STFC Consolidated Grant ST/N000749/1, while work at Imperial College London was supported by STFC Consolidated Grant ST/N000692/1. EJB was supported by a Royal Society Wolfson Research Merit Award. M.K.D. was supported by a Royal Society Research Professorship. T.J.B. was supported by STFC Quota Studentship ST/N504117/1. The authors thank S. Kellock and the Cassini magnetometer team at Imperial College for access to processed magnetic field data.

References

Achilleos, N., Guio, P., & Arridge, C. S. (2010). A model of force balance in Saturn's magnetodisc. *Monthly Notices of the Royal Astronomical Society*, *401*(4), 2349–2371. https://doi.org/10.1111/j.1365-2966.2009.15865.x

Alexeev, I. I., & Belenkaya, E. S. (2005). Modeling of the Jovian magnetosphere. *Annales Geophysicae*, *23*, 809–826. https://doi.org/10.5194/angeo-23-809-2005

Alexeev, I. I., & Feldstein, Y. I. (2001). Modeling of geomagnetic field during magnetic storms and comparison with observations. *Journal of Atmospheric and Solar-Terrestrial Physics*, *63*, 331–340. https://doi.org/10.1016/S1364-6826(00)00170-X

Alexeev, I. I., Kalegaev, V. V., Belenkaya, E. S., Bobrovnikov, S. Y., Bunce, E. J., Cowley, S. W. H., & Nichols, J. D. (2006). A global magnetic model of Saturn's magnetosphere and a comparison with Cassini SOI data. *Geophysical Research Letters*, *33*, L08101. https://doi.org/10.1029/2006GL02589

Andrews, D. J., Cecconi, B., Cowley, S. W. H., Dougherty, M. K., Lamy, L., Provan, G., & Zarka, P. (2011). Planetary period oscillations in Saturn's magnetosphere: Evidence in magnetic field phase data for rotational modulation of Saturn kilometric radiation emissions. *Journal of Geophysical Research*, *116*, A09206. https://doi.org/10.1029/2011JA016636

Andrews, D. J., Coates, A. J., Cowley, S. W. H., Dougherty, M. K., Lamy, L., Provan, G., & Zarka, P. (2010). Magnetospheric period oscillations at Saturn: Comparison of equatorial and high-latitude magnetic field periods with north and south SKR periods. *Journal of Geophysical Research*, *115*, A12252. https://doi.org/10.1029/2010JA015666

Arridge, C. S., Achilleos, N., Dougherty, M. K., Khurana, K. K., & Russell, C. T. (2006). Modeling the size and shape of Saturn's magnetopause with variable dynamic pressure. *Journal of Geophysical Research*, *111*, A11227. https://doi.org/10.1029/2005JA011574

Arridge, C. S., Khurana, K. K., Russell, C. T., Southwood, D. J., Achilleos, N., Dougherty, M. K., et al. (2008). Warping of Saturn's magnetospheric and magnetotail 1084 current sheets. *Journal of Geophysical Research*, *113*, A08217. https://doi.org/10.1029/2007JA012963

Arridge, C. S., Russell, C. T., Khurana, K. K., Achilleos, N., André, N., Rymer, A. M., et al. (2007). Mass of Saturn's magnetodisc: Cassini observations. *Geophysical Research Letters*, *34*, L09108. https://doi.org/10.1029/2006G028921

Arridge, C. S., Russell, C. T., Khurana, K. K., Achilleos, N., Cowley, S. W. H., Dougherty, M. K., et al. (2008). Saturn's magnetodisc current sheet. *Journal of Geophysical Research*, *113*, A04214. https://doi.org/10.1029/2007JA012540

Bradley, T. J., Cowley, S. W. H., Bunce, E. J., Melin, H., Nichols, J. D., Provan, G., et al. (2020). Saturn's nightside dynamics during Cassini's F ring and proximal orbits: Response to solar wind and planetary period oscillation modulations. *Journal of Geophysical. Research: Space Physics*, *125*, e2020JA027907. https://doi.org/10.1002/2020JA027907

Bradley, T. J., Cowley, S. W. H., Bunce, E. J., Smith, A. W., Jackman, C. J., & Provan, G. (2018). Planetary period modulation of reconnection bursts in Saturn's magnetotail. *Journal of Geophysical Research*, *123*, 9476–9507. https://doi.org/10.1002/2018JA025426

Bunce, E. J., Arridge, C. S., Cowley, S. W. H., & Dougherty, M. K. (2008). Magnetic field structure of Saturn's dayside magnetosphere and its mapping to the ionosphere: Results from ring current modelling. *Journal of Geophysical Research*, *113*, A02207. https://doi.org/10.1029/2007JA012538

Bunce, E. J., & Cowley, S. W. H. (2003). A note on the ring current in Saturn's magnetosphere: Comparison of magnetic data obtained during the Pioneer-11 and Voyager-1 and -2 fly-bys. *Annales Geophysicae*, *21*, 661–669.

Bunce, E. J., Cowley, S. W. H., Alexeev, I. I., Arridge, C. S., Dougherty, M. K., Nichols, J. D., & Russell, C. T. (2007). Cassini observations of the variation of Saturn's ring current parameters with system size. *Journal of Geophysical Research*, *112*, A10202. https://doi.org/10.1029/2007JA012275

Cao, H., Dougherty, M. K., Hunt, G., Provan, G., Cowley, S.W.H., Kellock, S., & Stevenson, D. J. (2020). The landscape of Saturn's internal magnetic field from the Cassini Grand Finale. *Icarus*, *344*, 113541. https://doi.org/10.1016/j.icarus.2019.113541

Carbary, J. F. (2019). A new ring current model for Saturn. *Journal of Geophysical Research: Space Physics*, *124*, 3378–3389. https://doi.org/10.1029/2019JA026560

Carbary, J. F., Achilleos, N., & Arridge, C. S. (2012). Statistical ring current of Saturn. *Journal of Geophysical Research*, *117*, A06223. https://doi.org/10.1029/2011JA017472

Carbary, J. F., & Mitchell, D. G. (2013). Periodicities in Saturn's magnetosphere. *Reviews of Geophysics*, *51*, 1–30. https://doi.org/10.1002/rog.20006

Connerney, J. E. P., Acuña, M. H., & Ness, N. F. (1981). Modeling the Jovian current sheet and inner magnetosphere. *Journal of Geophysical Research*, *86*, 8370–8384.

Connerney, J. E. P., Acuña, M. H., & Ness, N. F. (1981). Saturn's ring current and inner magnetosphere. *Nature*, *292*, 724–726.

Connerney, J. E. P., Acuña, M. H., & Ness, N. F. (1983). Currents in Saturn's magnetosphere. *Journal of Geophysical Research*, *88*, 8779–8789.

Cowley, S. W. H., Bunce, E. J., & Prangé, R. (2004). Saturn's polar ionospheric flows and their relation to the main auroral oval. *Annales Geophysicae*, *22*, 1379–1394.

Cowley, S. W. H., & Provan, G. (2017). Planetary period modulations of Saturn's magnetotail current sheet during northern spring: Observations and modeling. *Journal of Geophysical Research: Space Physics*, *122*, 6049–6077. https://doi.org/10.1002/2017JA023993

Cowley, S. W. H., Provan, G., Hunt, G. J., & Jackman, C. M. (2017). Planetary period modulations of Saturn's magnetotail current sheet: A simple illustrative mathematical model. *Journal of Geophysical Research: Space Physics*, *122*, 258–279. https://doi.org/10.1002/2016JA023367

Cowley, S. W. H., Wright, D. M., Bunce, E. J., Carter, A. C., Dougherty, M. K., Giampieri, G., et al. (2006). Cassini observations of planetary-period magnetic field oscillations in Saturn's magnetosphere: Doppleshifts and phase motion. *Geophysical Research Letters*, L07104. https://doi.org/10.1029/2005GL025522

Desch, M. D. (1982). Evidence for solar wind control of Saturn's radio emission. *Journal of Geophysical Research*, *87*, 4549–4554.

Desch, M. D., & Rucker, H. O. (1983). The relationship between Saturn kilometric radiation and the solar wind. *Journal of Geophysical Research*, *88*, 8999–9006.

Dougherty, M. K., Achilleos, N., Andre, N., Arridge, C. S., Balogh, A., Bertucci, C., et al. (2005). Cassini magnetometer observations during Saturn orbit insertion. *Science*, *307*, 1266–1270. https://doi.org/10.1126/science.1106098

Dougherty, M. K., Cao, H., Khurana, K. K., Hunt, G. J., Provan, G., Kellock, S., et al. (2018). Saturn's magnetic field Revealed by Cassini's Grand Finale. *Science*, *362*, eaat5434. https://doi.org/10.1126/science.aat5434

Dungey, J. W. (1961). Interplanetary field and the auroral zones. *Physical Review Letters*, *6*, 47.

Edwards, T. M., Bunce, E. J., & Cowley, S. W. H. (2001). A note on the vector potential of Connerney et al.'s model of the equatorial current sheet in Jupiter's magnetosphere. *Planetary and Space Science*, *49*, 1115–1123.

Giampieri, G., & Dougherty, M. K. (2004). Modeling of the ring current in Saturn's magnetosphere. *Annales. Geophysicae*, *22*, 653–659.

Gombosi, T. I., Armstrong, T. P., Arridge, C. S., Khurana, K. K., Krimigis, S. M., Krupp, N., et al. (2009). Persoon Saturn's magnetospheric configuration. In *Saturn from Cassini-Huygens*. (pp. 203–255). Springer Netherlands. https://doi.org/10.1007/978-1-4020-9217-6_9

Gurnett, D. A., Lecacheux, A., Kurth, W. S., Persoon, A. M., Groene, J. B., Lamy, L., et al. (2009). Discovery of a north-south asymmetry in Saturn's radio rotation period. *Geophysical Research Letters*, *36*, L16102. https://doi.org/10.1029/2009GL039621

Gurnett, D. A., Persoon, A. M., Groene, J. B., Kopf, A. J., Hospodarsky, G. B., & Kurth, W. S. (2009). A north-south difference in the rotation rate of auroral hiss at Saturn: Comparison to Saturn's kilometric radio emission. *Geophysical Research Letters*, *36*, L21108. https://doi.org/10.1029/2009GL040774

Hunt, G. J., Cowley, S. W. H., Provan, G., Bunce, E. J., Alexeev, I. I., Belenkaya, E. S., et al. (2015). Field-aligned currents in Saturn's northern nightside magnetosphere: Evidence for inter-hemispheric current flow associated with planetary period oscillations. *Journal of Geophysical Research: Space Physics*, *120*, 7552–7584. https://doi.org/10.1002/2015JA021454

Jackman, C. M., Lamy, L., Freeman, M. P., Zarka, P., Cecconi, B., Kurth, W. S., et al. (2009). On the character and distribution of lower-frequency radio emissions at Saturn and their relationship to substorm-like events. *Journal of Geophysical Research*, *114*, A08211. https://doi.org/10.1029/2008JA013997

Kanani, S. J., Arridge, C. S., Jones, G. H., Fazakerley, A. N., McAndrews, H. J., Sergis, N., et al. (2010). A new form of Saturn's magnetopause using a dynamic pressure balance model, based on in situ, multi-instrument Cassini measurements. *Journal of Geophysical Research*, *115*, A06207. https://doi.org/10.1029/2009JA014262

Kellett, S., Bunce, E. J., Coates, A. J., & Cowley, S. W. H. (2009). Thickness of Saturn's ring current determined from north-south Cassini passes through the current layer. *Journal of Geophysical Research*, *114*, A04209. https://doi.org/10.1029/2008JA013942

Khurana, K. K., Dougherty, M. K., Provan, G., Hunt, G. J., Kivelson, M. G., Cowley, S. W. H., et al. (2018). Discovery of atmospheric-wind driven electric currents in Saturn's magnetosphere in the gap between Saturn and its rings. *Geophysical Research Letters*, *45*(10), 10068–10074. https://doi.org/10.1002/2018GL078256

Kinrade, J., Badman, S. V., Paranicas, C., Mitchell, D. G., Arridge, C. S., Gray, R. L., et al. (2020). Tracking counterpart signatures in Saturn's auroras and ENAimagery during large✓scale plasmainjection events. *Journal of Geophysical Research: Space Physics*, *125*, e2019JA027542. https://doi.org/10.1029/2019JA027542

Kurth, W. S., Averkamp, T. F., Gurnett, D. A., Groene, J. B., & Lecacheux, A. (2008). An update to a Saturnian longitude system based on kilometric radio emissions. *Journal of Geophysical Research*, *113*, A05222. https://doi.org/10.1029/2007JA012861

Mardia, K. V., & Jupp, P. E. (2000). *Directional statistics*. Chichester: J. Wiley and Sons Ltd.

Mauk, B. H., Hamilton, D. C., Hill, T. W., Hospodarsky, G. B., Johnson, R. E., Paranicas, C., et al. (2009). Fundamental plasma processes in Saturn's magnetosphere. In M. K. Dougherty, L. W. Esposito, & S. M. Krimigis (Eds.), *Saturn from Cassini-Huygens* (pp. 281–331). Dordrecht: Springer.

McIlwain, C. E. (1961). Coordinates for mapping the distribution of magnetically trapped particles. *Journal of Geophysical Research*, *66*, 3681–3691. https://doi.org/10.1029/JZ066i011p03681

Mitchell, D. G., Krimigis, S. M., Paranicas, C. P., Brandt, P. C., Carbary, J. F., Roelof, E. C., et al. (2009). Recurrent energization of plasma in the midnight-to-dawn quadrant of Saturn's magnetosphere, and its relationship ion to auroral UV and radio. *Planetary and Space Science*, *57*, 1732–1742. https://doi.org/10.1016/j.pss.2009.04.002

Morooka, M.W., Modolo, R., Wahlund, J.-E., André, M., Eriksson, A.I., Persoon, A.M., et al. (2009). The electron density of Saturn's magnetosphere. *Annales Geophysicae*, *27*, 2971–2991.
Ness, N. F., Acuña, M. H., Behannon, K. W., Burlaga, L. F., Connerney, J. E. P., Lepping, R. P., & Neubauer, F. (1982). Magnetic field studies by Voyager 2: Preliminary results at Saturn. *Science*, *215*, 558–563.
Ness, N. F., Acuña, M. H., Lepping, R. P., Connerney, J. E. P., Behannon, K. W., Burlaga, L. F., & Neubauer, F. (1981). Magnetic field studies by Voyager 1: Preliminary results at Saturn. *Science*, *212*, 211–217.
Pensionerov, I. A., Alexeev, I. I., Belenkaya, E. S., Connerney, J. E. P., & Cowley, S. W. H. (2019). Model of Jupiter's current sheet with a piecewise current density. *Journal of Geophysical Research: Space Physics*, *124*, 1843–1854. https://doi.org/10.1029/2018JA026321
Persoon, A. M., Gurnett, D. A., Santolik, O., Kurth, W. S., Faden, J. B., Groene, J. B., et al. (2009). A diffusive equilibrium model for the plasma density in Saturn's magnetosphere. *Journal of Geophysical Research*, *114*, A04211. https://doi.org/10.1029/2008JA013912
Persoon, A. M., Kurth, W. S., Gurnett, D. A., Faden, J. B., Groene, J. B., Morooka, M. W., et al. (2020). The plasma distribution in Saturn's inner magnetosphere from 2.4 to 10 RS: A diffusive equilibrium model. *Journal of Geophysical Research: Space Physics*, *125*, e2019JA027545. https://doi.org/10.1029/2019JA027545
Provan, G., Andrews, D. J., Arridge, C. S., Coates, A. J., Cowley, S. W. H., Cox, G., et al. (2012). Dual periodicities in planetary-period magnetic field oscillations in Saturn's tail. *Journal of Geophysical Research*, *117*, A01209. https://doi.org/10.1029/2011JA017104
Provan, G., Andrews, D. J., Arridge, C. S., Cowley, S. W. H., Milan, S. E., Dougherty, M. K., & Wright, D. M. (2009). Polarization and phase of planetary period oscillations on high latitude field lines in Saturn's magnetosphere. *Journal of Geophysical Research*, *114*, A02225. https://doi.org/10.1029/2008JA013782
Provan, G., Andrews, D. J., Cecconi, B., Cowley, S. W. H., Dougherty, M. K., Lamy, L., & Zarka, P. (2011). Magnetospheric period magnetic field oscillations at Saturn: Equatorial phase 'jitter' produced by superposition of southern- and northern-period oscillations. *Journal of Geophysical Research*, *116*, A04225. https://doi.org/10.1029/2010JA016213
Provan, G., Cowley, S. W. H., Bradley, T. J., Bunce, E. J., Hunt, G. J., Cao, H., & Dougherty, M. K. (2019). Magnetic field observations on Cassini's proximal periapsis passes: Planetary period oscillations and mean residual fields. *Journal of Geophysical Research: Space Physics*, *124*, 8814–8864. https://doi.org/10.1002/2019JA026800
Provan, G., Cowley, S. W. H., Bradley, T. J., Bunce, E. J., Hunt, G. J., & Dougherty, M. K. (2018). Planetary period oscillations in Saturn's magnetosphere: Cassini magnetic field observations over the northern summer solstice interval. *Journal of Geophysical Research: Space Physics*, *123*, 3859–3899. https://doi.org/10.1002/2018JA025237
Provan, G., Cowley, S. W. H., Bunce, E. J., Bradley, T. J., Hunt, G. J., Cao, H., & Dougherty, M. K. (2019). Variability of intra-D ring azimuthal magnetic field profiles observed on Cassini's proximal periapsis passes. *Journal of Geophysical Research: Space Physics*, *124*, 379–404. https://doi.org/10.1002/2018JA026121
Ramer, K. M., Kivelson, M. G., Sergis, N., Khurana, K. K., & Jia, X. (2017). Spinning, breathing, and flapping: Periodicities in Saturn's middle magnetosphere. *Journal of Geophysical Research: Space Physics*, *122*, 393–416. https://doi.org/10.1002/2016JA023126
Reed, J. J., Jackman, C. M., Lamy, L., Kurth, W. S., & Whiter, D. K. (2018). Low-frequency extensions of the Saturn kilometric radiation as a proxy for magnetospheric dynamics. *Journal of Geophysical Research: Space Physics*, *123*, 443–463. https://doi.org/10.1002/2017JA024499
Richardson, J. D., & Sittler, E. C. (1990). A plasma density model for Saturn based on Voyager observations. *Journal of Geophysical Research*, *95*(A8), 12019. https://doi.org/10.1029/JA095iA08p12019
Roussos, E., Jackman, C. M., Thomsen, M. F., Kurth, W. S., Badman, S. V., Paranicas, C., et al. (2018). Solar energetic particles (SEP) and galactic cosmic rays (GCR) as tracers of solar wind conditions near Saturn: Event lists and applications. *Icarus*, *300*, 47–71. https://doi.org/10.1016/j.icarus.2017.08.040
Roussos, E., Krupp, N., Paranicas, C., Kollmann, P., Mitchell, D. G., Krimigis, S. M., et al. (2018). Heliospheric conditions at Saturn during Cassini's ring grazing and proximal orbits. *Geophysical Research Letters*, *45*, 10812–10818. https://doi.org/10.1029/2018GL078093
Russell, C. T. (2003). The structure of the magnetopause. *Planetary and Space Science*, *51*, 731–744.
Sergis, N., Arridge, C. S., Krimigis, S. M., Mitchell, D. G., Rymer, A. M., Hamilton, D. C., et al. (2011). Dynamics and seasonal variations in Saturn's magnetospheric plasma sheet, as measured by Cassini. *Journal of Geophysical Research*, *116*, A04203. https://doi.org/10.1029/2010JA016180
Sergis, N., Jackman, C. M., Thomsen, M. F., Krimigis, S. M., Mitchell, D. G., Hamilton, D. C., et al. (2017). Radial and local time structure of the Saturnian ring current, revealed by Cassini. *Journal of Geophysical Research: Space Physics*, *122*, 1803–1815. https://doi.org/10.1002/2016JA023742
Sittler, E. C., Andre, N., Blanc, M., Burger, M., Johnson, R. E., Coates, A. J., et al. (2008). Ion and neutral sources and sinks within Saturn's inner magnetosphere: Cassini results. *Planetary and Space Science*, *56*(1), 3–18. https://doi.org/10.1016/j.pss.2007.06.006
Sittler, E. C., Ogilvie, K. W., & Scudder, J. D. (1983). Survey of low-energy plasma electrons in Saturn's magnetosphere. *Journal of Geophysical Research*, *88*(A11), 8848–8870. https://doi.org/10.1029/JA088iA11p08847
Smith, E. J., Davis, L., Jones, D. E., Coleman, P. J., Colburn, D. S., Dyal, P., & Sonett, C. P. (1980). Saturn's Magnetosphere and its interaction with the solar wind. *Journal of Geophysical Research*, *85*, 5655–5674.
Sorba, A. M., Achilleos, N. A., Guio, P., Arridge, C. S., Pilkington, N. M., Masters, A., et al. (2017). Modeling the compressibility of Saturn's magnetosphere in response to internal and external influences. *Journal of Geophysical Research: Space Physics*, *122*, 1572–1589. https://doi.org/10.1002/2016JA023544
Sorba, A. M., Achilleos, N. A., Guio, P., Arridge, C. S., Sergis, N., & Dougherty, M. K. (2018). The periodic flapping and breathing of Saturn's magnetodisk during equinox. *Journal of Geophysical Research: Space Physics*, *123*, 8292–8316. https://doi.org/10.1029/2018JA025764
Sorba, A. M., Achilleos, N. A., Sergis, N., Guio, P., Arridge, C. S., & Dougherty, M. K. (2019). In D. J., & M. G. Kivelson (Ed.), Local time variation in the large-scale structure of Saturn's magnetosphere, (Vol. 124, pp. 7425–7441). https://doi.org/10.1029/2018JA026363
Southwood, D. J., & Kivelson, M. G. (1987). Magnetospheric interchange instability. *Journal of Geophysical Research*, *92*, 109–116.
Staniland, N. R., Dougherty, M. K., Master, A., Bunce, E. J., Staniland, N. R., & Dougherty, M. K. (2020). Determining the nominal thickness and variability of the magnetodisc current sheet at Saturn. *Journal of Geophysical Research: Space Physics*, *125*, e2020JA027794. https://doi.org/10.1029/2020JA027794
Tao, C., Kataoka, R., Fukunishi, H., Takahashi, Y., & Yokoyama, T. (2005). Magnetic field variations in the Jovian magnetotail induced by solar wind dynamic pressure enhancements. *Journal of Geophysical Research*, *110*, A11208. https://doi.org/10.1029/2004JA010959
Thomsen, M. F. (2013). Saturn's magnetospheric dynamics. *Geophysical Research Letters*, *40*, 5337–5344. https://doi.org/10.1002/2013GL057967
Thomsen, M. F., & Coates, A. J. (2019). Saturn's plasmapause: Signature of magnetospheric dynamics. *Journal of Geophysical Research: Space Physics*, *124*, 8804–8813. https://doi.org/10.1029/2019JA027075

Thomsen, M. F., Jackman, C. M., Cowley, S. W. H., Jia, X., Kivelson, M. G., & Provan, G. (2017). Evidence for periodic variations in the thickness of Saturn's nightside plasma sheet. *Journal of Geophysical Research: Space Physics*, *121*, 280–292. https://doi.org/10.1002/2016JA023368

Thomsen, M. F., Mitchell, D. G., Jia, X., Jackman, C. M., Hospodarsky, G., & Coates, A. J. (2015). Plasmapause formation at Saturn. *Journal of Geophysical Research: Space Physics*, *120*, 2571–2583. https://doi.org/10.1002/2015JA021008

Vasyliunas, V. M. (1983). Plasma distribution and flow. In A. J. Dessler (Eds.), *Physics of the Jovian Magnetosphere* (p. 395). Cambridge: Cambridge University Press.

Young, D. T., Berthelier, J.-J., Blanc, M., Burch, J. L., Coates, A. J., Goldstein, R., et al. (2005). Composition and dynamics of plasma in, Saturn's magnetosphere. *Science*, *307*, 1262–1266.

Zieger, B., & Hansen, K. C. (2008). Statistical validation of a solar wind propagation model from 1 to 1952 10 AU. *Journal of Geophysical Research*, *113*, A08107. https://doi.org/10.1029/2008JA013046